Geophysical Journal International

Geophys. J. Int. (2009) **179,** 1429–1457 doi: 10.1111/j.1365-246X.2009.04367.x

On the electromagnetic fields produced by marine frequency domain controlled sources

Alan D. Chave

Deep Submergence Laboratory, Department of Applied Ocean Physics and Engineering, Woods Hole Oceanographic Institution, Woods Hole, MA 02543*, USA. E-mail: achave@whoi.edu*

Accepted 2009 August 17. Received 2009 August 17; in original form 2009 January 26

SUMMARY

In recent years, marine controlled source electromagnetics (CSEM) has found increasing use in hydrocarbon exploration due to its ability to detect thin resistive zones beneath the seafloor. Although it must be recognized that the quantitative interpretation of marine CSEM data over petroleum-bearing formations will typically require 2-D surveys and 2-D or 3-D modelling, the use of the 1-D approximation is useful under some circumstances and provides considerable insight into the physics of marine CSEM. It is the purpose of this paper to thoroughly explore the 1-D solutions for all four fundamental source types—vertical and horizontal, electric and magnetic dipole (VED, HED, VMD and HMD)—using a set of canonical reservoir models that encompass brine to weak to strong hydrocarbon types. The paper introduces the formalism to solve the Maxwell equations for a 1-D structure in terms of independent and unique toroidal and poloidal magnetic modes that circumscribe the salient diffusion physics. Green's functions for the two modes from which solutions for arbitrary source current distributions can be constructed are derived and used to obtain the electromagnetic (EM) fields produced by finite VED, HED, VMD and HMD sources overlying an arbitrary 1-D electrical structure. Field behaviour is analysed using the Poynting vector that represents the time-averaged flow of energy through the structure and a polarization ellipse decomposition of the triaxial seafloor EM field that is a complete field description. The behaviour of the two EM modes using unimodal VED and VMD sources is presented. The paper closes by extending these results to the bimodal HED and HMD sources.

Key words: Electromagnetic theory; Marine electromagnetics.

1 INTRODUCTION

The theory of propagation for ELF/SLF (<300 Hz) electromagnetic (EM) fields through, under and over the ocean from a submerged source has been investigated for more than fifty years as a means for communication, underwater detection and geophysical exploration (e.g. Mott & Biggs 1963; Bannister 1968; Chave *et al.* 1990). Pioneering measurements by Cox *et al.* (1978) showed that the natural background noise in the electric field at frequencies around 1 Hz is extremely low ($\sim$1 pV m^{-1}), suggesting that the weak fields induced within Earth by a near-seafloor artificial source could be detected at large (many kilometres) source–receiver offsets. This led to the development of practical geophysical exploration methods based on seabed-to-seabed propagation of low frequency EM fields from controlled sources, as reviewed by Chave *et al.* (1991) and Edwards (2005). A variety of techniques have been developed. A vertical electric dipole (VED) source and horizontal magnetic field receivers have been used for sounding to depths of several kilometres on the continental shelf, over permafrost and on a mid-ocean ridge (Edwards *et al.* 1981, 1985, 1988; Evans *et al.* 1998). A horizontal electric dipole (HED) source and receivers were employed by Young & Cox (1981), Cox *et al.* (1986) and Constable & Cox (1996) to investigate the electrical conductivity of the oceanic lithosphere to depths of tens of kilometres, revealing a very low ($\sim 10^{-5}$ S m^{-1}) value beneath the mid-plate oceanic crust. More recently, MacGregor *et al.* (1998, 2001) used the technique to investigate the structure beneath a slow spreading mid-ocean ridge and a backarc basin. Towed time-domain HED−HED technology was developed for mapping methane hydrates on the continental shelf by Yuan & Edwards (2000). Finally, Evans (2007) describes a towed frequency-domain horizontal magnetic dipole (HMD) source with magnetic field receivers for the study of shallow (tens of metres) sedimentary structures.

There has been interest in using controlled source electromagnetics (CSEM) for petroleum exploration and especially for direct hydrocarbon detection, since the 1930s, as reviewed by Nekut & Spies (1989). Much of the early work was based on the belief that CSEM

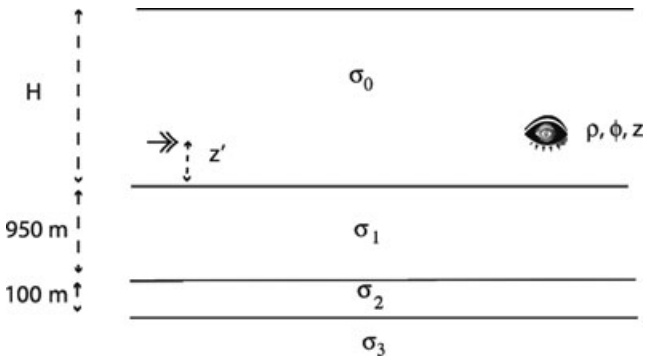

Figure 1. The canonical reservoir model used throughout this paper. The source (double arrow) is located at (0, 0, z') and the observation point (eye) is at (ρ, ϕ, z). The ocean layer of thickness H and conductivity $\sigma_0 = 3.2$ S m^{-1} is overlain by the insulating atmosphere and underlain by a two layer structure in turn underlain by a half-space. In all cases, $\sigma_1 = \sigma_3 = 0.5$ S m^{-1}. The weak hydrocarbon reservoir model has $\sigma_2 = 0.05$ S m^{-1}, whereas the strong reservoir model has $\sigma_2 = 0.017$ S m^{-1}. The brine reservoir model has $\sigma_2 = 5$ S m^{-1}.

could be used to detect EM reflections that was commercialized as the Eltran method in the 1940s (Horton 1946; Yost 1952) and subsequently discredited. Combined with the increasing success of seismic reflection as the standard tool for hydrocarbon exploration through the 1990s, this led to a declining level of interest in EM within the petroleum industry. A major exception occurred in the former USSR, where EM methods played an important role (Spies 1983; Berdichevsky 1994).

It has long (e.g. Martin *et al.* 1938) been known that hydrocarbon zones are typically resistive relative to the substrate in which they are embedded, although there are exceptions. Using well log data, Garg & Keller (1984) showed that a sandstone reservoir surrounded by shale provides the highest resistivity contrast, whereas in a relatively impermeable carbonate sequence, the resistivity contrast can actually be reversed (i.e. the reservoir is conductive relative to the substrate) unless hydrocarbon saturation is very high. In addition, in many sedimentary basins, anomalous material produced through chemical alteration by upward migration of hydrocarbons results in a reduction of the conductivity in the rock overlying a producing layer (Oehler & Sternberg 1984; Nekut & Spies 1989). Consequently, a resistive zone detected using an EM method may have a greater physical extent than the actual hydrocarbon-bearing formation.

Passalaqua (1983) showed theoretically that a thin resistive hydrocarbon zone could be sensed using CSEM and several groups attempted to exploit this property on land through the 1990s (e.g. Keller *et al.* 1995; Strack & Vozoff 1996). Meju (2002) provides a recent survey of these efforts. Further, it has long been recognized that marine CSEM is preferentially sensitive to thin resistive zones (e.g. Cheesman *et al.* 1987), including those containing hydrocarbons (Cox & Chave 1983; Srnka 1986). Subsequently, Ellingsrud *et al.* (2002) demonstrated that a producing offshore petroleum field could be mapped with the same HED−HED technique and apparatus utilized in academia over the previous twenty years. This resulted in the rapid commercial expansion of marine CSEM that continues to this day, along with a concomitant flurry of presentations, publications and patents about the method. Constable & Srnka (2007) provide a historical perspective on these developments.

Although it must be recognized that the quantitative interpretation of marine CSEM data over petroleum-bearing formations will typically require 2-D surveys and 2-D or 3-D modelling, the use of the 1-D approximation is useful under some circumstances and provides considerable insight into the physics of marine CSEM. It is the purpose of this paper to thoroughly explore the 1-D solutions for all four fundamental source types—VED, HED, vertical magnetic dipole (VMD) and HMD—using the canonical reservoir model shown in Fig. 1. This model incorporates a 100 m thick reservoir layer centered at 1000 m depth in a substrate with an electrical conductivity of 0.5 S m^{-1} (resistivity of 2 Ω-m). The reservoir layer has a conductivity of 5 S m^{-1} (resistivity of 0.2 Ω-m) representing brine, 0.05 S m^{-1} (resistivity of 20 Ω-m) representing a weak hydrocarbon zone and 0.017 S m^{-1} (resistivity of 60 Ω-m) representing a strong hydrocarbon zone. The conductivity contrast between the substrate and reservoir for the hydrocarbon models ranges from 10:1 to 30:1, smaller than the 100:1 value that is often used (e.g. Constable & Weiss 2006; Um & Alumbaugh 2007). Although 100:1 or higher conductivity contrasts have been observed in producing hydrocarbon areas (e.g. the Troll gas field off Norway; Johansen *et al.* 2005), a lower value is more typical. Although of limited physical significance in marine CSEM, the electric permittivity ε has the free space value throughout the structure except in water, where it is about 80 times larger.

The remainder of this paper is organized into ten sections and one appendix. Section 2 outlines a formalism to solve the Maxwell equations for a 1-D structure in terms of two independent and unique modes that circumscribe the salient diffusion physics. Section 3 presents Green's functions for the two modes from which solutions for arbitrary source current distributions can be constructed. Sections 4–7 contain derivations of the EM fields produced by finite HED, VED, VMD and HMD sources overlying an arbitrary 1-D electrical structure. Section 8 defines the Poynting vector that represents the time-averaged flow of energy through a structure and a polarization ellipse decomposition of a triaxial EM field that is a complete field description. Section 9 describes the behaviour of the two EM modes using unimodal VED and VMD sources. Section 10 extends these results to the bimodal HED and HMD sources. Section 11 summarizes the results. An appendix contains the derivation of the modal representation from first principles.

2 GOVERNING EQUATIONS

In a fixed reference frame, neglecting advected charge and polarization current and assuming that the magnetic permeability is invariant, Ampere's Law with both the displacement and conduction currents retained may be written

$$\tau \partial_t \mathbf{E} + \mathbf{E} = \frac{1}{\mu\sigma} \nabla \times \mathbf{B}, \tag{1}$$

where $\mathbf{B}$ is the magnetic induction, $\mathbf{E}$ is the electric field, μ is the magnetic permeability (assumed to be that of free space throughout this paper) and σ is the electrical conductivity. The charge relaxation time is $\tau = \varepsilon/\sigma$. Eq. (1) may be regarded as a simple first-order differential equation for $\mathbf{E}$ with driving term given by the right-hand side. It is easily integrated to give

$$\mathbf{E}(\mathbf{r}, t) = \mathbf{E}(\mathbf{r}, 0)\, \mathrm{e}^{-t/\tau} + \frac{1}{\tau} \int_0^t \mathrm{d}s\, \mathrm{e}^{-(t-s)/\tau} \frac{1}{\mu\sigma} \nabla \times \mathbf{B}(\mathbf{r}, s). \tag{2}$$

The electric field on the left of (2) is independent of the initial condition after a few times τ, and thereafter is the convolution of $\nabla \times \mathbf{B}/\mu\sigma$ with an exponential term whose decay constant is the charge relaxation time, resulting in temporal averaging. Using the estimates for σ and ε given for the canonical reservoir model of Fig. 1, in the ocean τ is about 0.2 ns, in the overburden τ is about 0.02 ns, in a hydrocarbon reservoir τ is 0.2−2 ns, and in a brine reservoir τ is about 0.1 ns. All of these values are very small compared to a typical period (of order 1 s) used in marine CSEM, so that the averaging is unimportant, and the electric field $\mathbf{E}$ in (2) is effectively given by $\nabla \times \mathbf{B}/\mu\sigma$, yielding the pre-Maxwell limit where displacement current is negligible compared to conduction current.

Further, it is not necessary to consider displacement current in the insulating air above the ocean provided that the source–receiver offset is small compared to the free space wavelength. For a frequency range of 0.01−100 Hz, encompassing that which may practically be used for CSEM in the ocean, the free space wavelength ranges from 3000 to 30 000 000 km and hence displacement current effects in the air are also negligible given that the source–receiver offset in marine CSEM is typically well under 100 km. Thus, the pre-Maxwell equations are sufficient throughout the structure of interest.

The pre-Maxwell equations are given by

$$\nabla \cdot \mathbf{B} = 0 \tag{3}$$

$$\nabla \times \mathbf{E} + \partial_t \mathbf{B} = 0 \tag{4}$$

$$\nabla \times \mathbf{B} - \mu\sigma \mathbf{E} = \mu \mathbf{J}^0, \tag{5}$$

where $\mathbf{J}^0$ is an extrinsic (source) electric current density.

The role of electric charge on surfaces in the pre-Maxwell limit is frequently misunderstood. Neglect of the displacement current in (5) requires that the electric current density $\mathbf{J} = \sigma\mathbf{E} + \mathbf{J}^0$ be divergence-free and hence the time rate of change of charge density is zero. In fact, the electric currents that distribute charge occur on a time scale given by the charge relaxation time τ that has been shown to be very small compared to a typical period used in marine CSEM and hence their current fluctuations do not produce a magnetic field. However, the electric fields produced by charges that move into place on boundaries with seemingly infinite speed are quite important and are not removed in the pre-Maxwell limit.

Define a coordinate system with $\hat{z}$ positive upward and zero at Earth's surface and assume that the electrical conductivity σ varies only in this direction. Eqs (3)–(5) will be solved for a variety of source geometries in terms of poloidal and toroidal magnetic (hereafter PM and TM, respectively) modes based on a Helmholtz representation of a vector field, as thoroughly described by Backus (1986). The modal form of the fields is more useful than the standard vector potential because it reduces the physics into two relatively simple and independent components. The PM mode is characterized by electric currents flowing in horizontal planes that couple purely by induction and has no vertical electric field component. The TM mode is associated with electric currents that may flow in planes containing the vertical, couples both inductively and galvanically and has no vertical magnetic field component.

Using the Helmholtz representation theorem, the source current density $\mathbf{J}^0$ may be written in terms of toroidal, consoidal and vertical parts

$$\mathbf{J}^0 = \hat{z} \times \nabla_h \Upsilon + \nabla_h T + \Xi \hat{z}, \tag{6}$$

where $\hat{z} \times \nabla_h$ and ∇_h are the surface curl and surface gradient operators, Ξ is the vertical component of the source current, and Υ and T are scalar functions that are unique except for additive constants. The toroidal and consoidal source current scalars satisfy

$$\nabla_h^2 \Upsilon = \left(\nabla_h \times \mathbf{J}_h^0\right) \cdot \hat{z} \tag{7}$$

$$\nabla_h^2 T = \nabla_h \cdot \mathbf{J}_h^0, \tag{8}$$

where ∇_h^2 is the surface Laplacian. By transforming the results in Backus (1986) from a spherical to a planar geometry, it can be shown that $\langle (\nabla_h \times \mathbf{J}_h^0) \cdot \hat{\mathbf{z}} \rangle = \langle \nabla_h \cdot \mathbf{J}_h^0 \rangle = 0$, where $\langle\rangle$ denotes the average over a plane defined as

$$\langle f(x, y) \rangle = \lim_{L \to \infty} \frac{1}{L^2} \int_{-L}^{L} \int_{-L}^{L} f(x, y)\, \mathrm{d}x\, \mathrm{d}y. \tag{9}$$

Consequently, the constants in Υ and T may be specified by requiring that $\langle \Upsilon \rangle = \langle T \rangle = 0$.

Using the properties of analytic functions of a complex variable (Appendix), it can be shown that the magnetic induction and electric field may be written

$$\mathbf{B} = \hat{z} \times \nabla_h \Pi + \nabla_h \partial_z \Psi - \nabla_h^2 \Psi \hat{z} \tag{10}$$

$$\mathbf{E} = \hat{z} \times \nabla_h \partial_t \Psi - \nabla_h \left(\partial_z \Pi + \mu T\right)/\mu\sigma + \left(\nabla_h^2 \Pi - \mu \Xi\right)/\mu\sigma \hat{z}, \tag{11}$$

where the PM and TM mode scalar functions satisfy the differential equations

$$\nabla^2 \Psi - \mu\sigma \partial_t \Psi = \mu \Upsilon \tag{12}$$

$$\nabla_h^2 \Pi + \sigma \partial_z \left(\frac{\partial_z \Pi}{\sigma}\right) - \mu\sigma \partial_t \Pi = \mu \Xi - \mu\sigma \partial_z \left(\frac{T}{\sigma}\right), \tag{13}$$

under the condition that $\langle \Psi \rangle = \langle \Pi \rangle = 0$ using (9). The PM mode is associated with the toroidal part of the source current, whereas the TM mode is driven by its vertical and consoidal elements.

The usual boundary conditions on the horizontal components of the electric and magnetic fields must be satisfied at horizontal interfaces, with the latter requiring inclusion of the source current when it is located in the interface. These in turn require continuity of Ψ, $\partial_z \Psi - \mu \Upsilon$, $\Pi + \mu T$ and $(\partial_z \Pi + \mu T)/\mu\sigma$. Because the boundary conditions are not coupled, the PM and TM modes represented by solutions of (12) and (13) are independent. Further, the condition that $\langle \Psi \rangle = \langle \Pi \rangle = 0$ guarantees that the two modes are unique and hence can be examined separately to understand the salient physics.

Forced oscillations of energy in a diffusive medium such as (12) and (13) describe are sometimes called diffusion waves (Mandelis 2006), and it is common in the geophysical literature to refer to CSEM fields using wave equation terminology. However, both (12) and (13) are parabolic diffusion equations rather than hyperbolic wave equations. In one dimension, a parabolic equation has only a single family of characteristic curves (lines of constant t), whereas a hyperbolic equation has two such families (lines of constant $x \pm ct$, where c is the phase velocity). Because they are not invariant under the transformation $t \to -t$, solutions to parabolic equations evolve unidirectionally forward in time simultaneously at all points away from a source. This set of traits precludes the existence of reflection (and concomitantly, refraction) at interfaces, as well as the use of ray physics. Mandelis *et al.* (2001) summarize the arguments. Consequently, terminology from and analogies to wave phenomena will be avoided in the sequel.

Although the derivation presented here requires only that the electrical conductivity σ vary with depth, the formalism extends in a straightforward manner to the cases where the magnetic permeability μ also varies with depth or the conductivity is transversely isotropic (i.e. has different values in the horizontal and vertical directions).

3 PM AND TM MODE GREEN'S FUNCTIONS

The time dependence of all variables will be taken as $\mathrm{e}^{-i\omega t}$ where ω is the angular frequency. It will be more convenient to work with the horizontal Fourier transforms of the modal differential eqs (12) and (13) using the convention

$$\tilde{f}(\eta,\xi) = \int_{-\infty}^{\infty} \int_{-\infty}^{\infty} f(x,y)\, \mathrm{e}^{i(\eta x + \xi y)}\, \mathrm{d}x\, \mathrm{d}y, \tag{14}$$

$$f(x,y) = \frac{1}{(2\pi)^2} \int_{-\infty}^{\infty} \int_{-\infty}^{\infty} \tilde{f}(\eta,\xi)\, \mathrm{e}^{-i(\eta x + \xi y)}\, \mathrm{d}\eta\, \mathrm{d}\xi, \tag{15}$$

where η and ξ are horizontal wavenumbers. Further analysis will be confined to the situation where a horizontal current source is not located in the seafloor interface to avoid boundary condition complexity. Green's functions solutions to the Fourier transforms of (12) and (13) for a constant conductivity ocean extending over $-H \le z \le 0$ are given by Chave & Luther (1990, Appendix B)

$$g_{\psi\{\pi\}}(z,z') = -\frac{\mathrm{e}^{-\beta_0|z-z'|} + \Omega_{\mathrm{L}}^{\mathrm{PM\{TM\}}}\, \mathrm{e}^{-2\beta_0 H}\, \mathrm{e}^{-\beta_0(z+z')} + \Omega_{\mathrm{U}}^{\mathrm{PM\{TM\}}}\, \mathrm{e}^{\beta_0(z+z')} + \Omega_{\mathrm{U}}^{\mathrm{PM\{TM\}}} \Omega_{\mathrm{L}}^{\mathrm{PM\{TM\}}}\, \mathrm{e}^{-2\beta_0 H}\, \mathrm{e}^{\beta_0|z-z'|}}{2\beta_0 \left(1 - \Omega_{\mathrm{U}}^{\mathrm{PM\{TM\}}} \Omega_{\mathrm{L}}^{\mathrm{PM\{TM\}}}\, \mathrm{e}^{-2\beta_0 H}\right)}, \tag{16}$$

where $k = \sqrt{\eta^2 + \xi^2}$ is the magnitude of the horizontal wavenumber, σ_0 is the electrical conductivity of the water layer, $\beta_0 = \sqrt{k^2 - i\omega\mu\sigma_0}$ is the ocean diffusion parameter and Ω_a^b are complex, wavenumber-dependent diffusion interaction coefficients at $z = -H$ ($a = L$) and $z = 0$ ($a = U$) for the $b =$ PM or TM mode. Note that $\Omega_U^{\mathrm{TM}} = -1$ if $z = 0$ is Earth's surface overlain by the atmosphere due to the requirement that the TM mode magnetic field vanish at and beyond insulating boundaries, whereas $\Omega_U^{\mathrm{PM}} = (\beta_0 - k)/(\beta + k)$ under the same condition.

Chave & Luther (1990, Appendix C) give stable recursive expressions for the lower diffusion interaction coefficient when Earth is represented as a stack of N layers of variable thickness h_i and conductivity σ_i terminated by a half-space that may be insulating, conducting, or a perfect conductor. These are

$$\Omega_i^{\mathrm{PM}} = \frac{\alpha_i + \mathrm{e}^{-2\beta_{i+1}h_{i+1}}\, \Omega_{i+1}^{\mathrm{PM}}}{1 + \alpha_i \mathrm{e}^{-2\beta_{i+1}h_{i+1}}\, \Omega_{i+1}^{\mathrm{PM}}}$$

$$\Omega_i^{\mathrm{TM}} = \frac{\chi_i + \mathrm{e}^{-2\beta_{i+1}h_{i+1}}\, \Omega_{i+1}^{\mathrm{TM}}}{1 + \chi_i \mathrm{e}^{-2\beta_{i+1}h_{i+1}}\, \Omega_{i+1}^{\mathrm{TM}}}, \tag{17}$$

where the interface interaction coefficients are given by

$$\alpha_i = \frac{\beta_i - \beta_{i+1}}{\beta_i + \beta_{i+1}}$$
$$\chi_i = \frac{\beta_i \sigma_{i+1} - \beta_{i+1}\sigma_i}{\beta_i \sigma_{i+1} + \beta_{i+1}\sigma_i}. \tag{18}$$

The diffusion interaction coefficients in (16) are obtained when $i = 0$. The PM mode diffusion interaction coefficient is initialized at $z = -z_N$ with α_N for a conducting or insulating half-space or -1 for a perfect conductor, whereas the TM mode diffusion interaction coefficient is initialized with χ_N for a conducting half-space, 1 for a perfect conductor or -1 for an insulator.

Using the Green's functions, solutions to the Fourier domain versions of (12) and (13) for a general source may be written

$$\tilde{\Psi}(z) = \mu \int_{-H}^{0} g_\psi(z, z')\tilde{\Upsilon}(z')\,\mathrm{d}z' \tag{19}$$

$$\tilde{\Pi}(z) = \mu \int_{-H}^{0} g_\pi(z,\, z')\tilde{\Xi}(z')\,\mathrm{d}z' + \mu \int_{-H}^{0} \partial_{z'} g_\pi(z, z')\tilde{T}(z')\,\mathrm{d}z', \tag{20}$$

where the second term in (20) is obtained after a single integration by parts. Solutions for the EM fields follow by taking inverse Fourier transforms using (15) and computing the appropriate horizontal and vertical derivatives. Note that the vertical derivatives (either in z or z') of the Green's functions, appear in some of the field expressions for each source type. Care must be taken in obtaining these, as they are discontinuous by ± 1 at $z = z'$. In addition, the TM mode horizontal electric field for an HED and horizontal magnetic field for an HMD contain the mixed second derivative of a Green's function that possesses a delta function discontinuity at $z = z'$, and may be written $\partial_z \partial_{z'} g_{\psi\{\pi\}}(z, z') = g^{\dagger}_{\psi\{\pi\}}(z, z') - \delta(z - z')$, where $g^{\dagger}_{\psi\{\pi\}}(z, z')$ is continuous.

Although the Green's functions in (16) are specific to a source located within the ocean, they can easily be converted to cover a source located at or above Earth's surface by replacing z and z' with $z - H$ and $z' - H$, respectively. Taking the limit $H \to \infty$ in the transformed version of (16) yields solutions for an infinitely thick top layer appropriate at Earth's surface or for an ocean that is electrically thick

$$g_{\psi\{\pi\}}(z, z') = -\left(\mathrm{e}^{-\beta_0|z-z'|} + \Omega_L^{\mathrm{PM\{TM\}}}\mathrm{e}^{-\beta_0(z+z')}\right)/2\beta_0. \tag{21}$$

In addition, the EM fields within the layered structure may easily be derived by matching solutions to the homogeneous forms of the spatial Fourier transforms of (12) and (13) at the seafloor to the Green's function using the appropriate boundary conditions. These may be propagated down to the depth of interest. Such solutions will be used to estimate the Poynting vector throughout the structure in Sections 9 and 10.

4 HORIZONTAL ELECTRIC DIPOLE SOURCE

The HED source, along with horizontal electric receivers, has long been used for marine CSEM and remains the configuration of choice for hydrocarbon applications. Chave & Cox (1982) derived expressions for the EM fields from an HED source and the treatment below builds on this foundation.

A point source electric dipole is oriented in the $\hat{x}$ direction and located at $(x', 0, z')$, so that the source electric current density is given by $\mathbf{J}^0 = p\delta(x - x')\delta(y)\delta(z - z')\hat{x}$, where p is the source moment given by the product of source current and infinitesimal dipole length $I\,\mathrm{d}x'$. Applying (14) to (7) and (8), the Fourier domain toroidal and consoidal source current scalars are given by

$$\tilde{\Upsilon}(z) = -\frac{ip\xi}{k^2}\mathrm{e}^{i\eta x'}\delta(z - z') \tag{22}$$

$$\tilde{T}(z) = \frac{ip\eta}{k^2}\mathrm{e}^{i\eta x'}\delta(z - z'), \tag{23}$$

whereas the vertical current term in (6) vanishes. Consequently, the HED induces both PM and TM modes within conductive media. Taking inverse Fourier transforms, it is easy to show that $\langle\Upsilon\rangle = \langle T\rangle = 0$ and hence the constants in the solutions to (7) and (8) are appropriately constrained.

The corresponding Fourier domain PM and TM mode scalar functions are given by

$$\tilde{\Psi}(z) = -\frac{i\mu p\xi}{k^2}\mathrm{e}^{i\eta x'}g_\psi(z, z') \tag{24}$$

$$\tilde{\Pi}(z) = \frac{i\mu p\eta}{k^2}\mathrm{e}^{i\mu x'}\partial_{z'}g_\pi(z, z'). \tag{25}$$

The inverse transform of (24)–(25) must average to zero on a given plane. This may be accomplished by replacing g_ψ and $\partial_{z'}g_\pi$ with $h_\psi = g_\psi - g^0_\psi$ and $\partial_{z'}h_\psi = \partial_{z'}g_\pi - \partial_{z'}g^0_\pi$, respectively, where the superscript 0 refers to the Green's function with $k = 0$. With this transformation, the PM and TM mode scalars are unique, as are the modal electric and magnetic field components derived from them.

The spatial domain counterparts to (24)–(25) are given by

$$\Psi(\mathbf{r}, \mathbf{r}') = \frac{\mu p}{4\pi^2}\partial_y \int_{-\infty}^{\infty}\int_{-\infty}^{\infty} \frac{h_\psi(z, z')}{k^2}\, e^{-i(\eta(x-x')+\xi y)}\,\mathrm{d}\eta\,\mathrm{d}\xi, \tag{26}$$

$$\Pi(\mathbf{r},\mathbf{r}') = -\frac{\mu p}{4\pi^2}\partial_x \int_{-\infty}^{\infty}\int_{-\infty}^{\infty} \frac{\partial_{z'} h_\pi(z,\, z')}{k^2}\, \mathrm{e}^{-i(\eta(x-x')+\xi y)}\, \mathrm{d}\eta\, \mathrm{d}\xi, \tag{27}$$

where $\mathbf{r}$ and $\mathbf{r}'$ are the observation and source points, respectively. The Green's functions (16) and their vertical derivatives are azimuthally symmetric. Consequently, converting from Cartesian to polar coordinates, where $(x, y) = \rho\,(\cos\phi, \sin\phi)$ and $(\eta, \xi) = k\,(\cos\theta, \sin\theta)$, so that $\mathrm{d}\eta\ \mathrm{d}\xi = k\ \mathrm{d}k\ \mathrm{d}\theta$, and applying Poisson's formula

$$\frac{1}{2\pi}\int_0^{2\pi} \mathrm{e}^{\pm ik\zeta\cos(\theta-\vartheta)}\, \mathrm{d}\theta = J_0\,(k\zeta), \tag{28}$$

where ϑ is an arbitrary angle, $J_0(k\zeta)$ is a Bessel function of the first kind of order 0, and $\zeta^2 = (x - x')^2 + y^2 = \rho^2 + x'^2 - 2\rho\, x'\cos\phi$, reduces (26)–(27) to Hankel transforms

$$\Psi(\mathbf{r},\mathbf{r}') = \frac{\mu p}{2\pi}\int_0^{\infty} \frac{h_\psi(z,z')}{k}\partial_y J_0\,(k\zeta)\ \mathrm{d}k \tag{29}$$

$$\Pi(\mathbf{r},\mathbf{r}') = -\frac{\mu p}{2\pi}\int_0^{\infty} \frac{\partial_{z'} h_\pi(z,z')}{k}\partial_x J_0(k\zeta)\,\mathrm{d}k. \tag{30}$$

The field components follow by applying (10)–(11) to (29)–(30). The resulting algebra is tedious, but is simplified by using cylindrical coordinates. Tabulating the necessary derivatives of the Bessel function terms yields

$$\begin{aligned}
&\partial_x J_0(k\zeta) = -k\partial_x\zeta J_1(k\zeta) \quad [-k\cos\phi J_1(k\rho)]\\
&\partial^2_{\rho x} J_0(k\zeta) = -k\left(k\partial_x\zeta\partial_\rho\zeta J_0(k\zeta) + \left(\partial^2_{\rho x}\zeta - \partial_x\zeta\partial_\rho\zeta/\zeta\right) J_1(k\zeta)\right) \quad [-k\cos\phi\,(kJ_0(k\rho) - J_1(k\rho)/\rho)]\\
&\frac{1}{\rho}\partial^2_{\phi x} J_0(k\zeta) = -k\left(k\partial_x\zeta\frac{1}{\rho}\partial_\phi\zeta J_0(k\zeta) + \left(\frac{1}{\rho}\partial^2_{\phi x}\zeta - \partial_x\zeta\frac{1}{\rho}\partial_\phi\zeta/\zeta\right) J_1(k\zeta)\right) \quad \left[\frac{k\sin\phi}{\rho}J_1(k\rho)\right]\\
&\partial_y J_0(k\zeta) = -k\partial_y\zeta J_1(k\zeta) \quad [-k\sin\phi J_1(k\rho)]\\
&\partial^2_{\rho y} J_0(k\zeta) = -k\left(k\partial_y\zeta\partial_\rho\zeta J_0(k\zeta) + \left(\partial^2_{\rho y}\zeta - \partial_y\zeta\partial_\rho\zeta/\zeta\right) J_1(k\zeta)\right) \quad [-k\sin\phi\,(kJ_0(k\rho) - J_1(k\rho)/\rho)]\\
&\frac{1}{\rho}\partial^2_{\phi y} J_0(k\zeta) = -k\left(k\partial_y\zeta\frac{1}{\rho}\partial_\phi\zeta J_0(k\zeta) + \left(\frac{1}{\rho}\partial^2_{\phi y}\zeta - \partial_y\zeta\frac{1}{\rho}\partial_\phi\zeta/\zeta\right) J_1(k\zeta)\right) \quad \left[-\frac{k\cos\phi}{\rho}J_1(k\rho)\right],\\
&\nabla^2_h\partial_y J_0(k\zeta) = k^3\partial_y\zeta J_1(k\zeta) \quad \left[k^3\sin\phi J_1(k\rho)\right]\\
&\nabla^2_h\partial_x J_0(k\zeta) = k^3\partial_x\zeta J_1(k\zeta) \quad \left[k^3\cos\phi J_1(k\rho)\right],
\end{aligned} \tag{31}$$

where the term in square brackets is the result for a centered dipole ($x' = 0$). The derivatives of ζ are

$$\begin{aligned}
&\partial_\rho\zeta = \frac{\rho^2 - xx'}{\rho\zeta} \quad [1]\\
&\frac{1}{\rho}\partial_\phi\zeta = \frac{yx'}{\rho\zeta} \quad [0]\\
&\partial_x\zeta = \frac{x - x'}{\zeta} \quad [\cos\phi]\\
&\partial_y\zeta = \frac{y}{\zeta} \quad [\sin\phi]\\
&\partial^2_{\rho x}\zeta = \frac{\zeta^2 x - (x - x')(\rho^2 - xx')}{\rho\zeta^3} \quad [0]\\
&\frac{1}{\rho}\partial^2_{\phi x}\zeta = -\frac{y(\zeta^2 + x'(x - x'))}{\rho\zeta^3} \quad \left[-\frac{\sin\phi}{\rho}\right]\\
&\partial^2_{\rho y}\zeta = \frac{y(\zeta^2 - \rho^2 + xx')}{\rho\zeta^3} \quad [0]\\
&\frac{1}{\rho}\partial^2_{\phi y}\zeta = \frac{x\zeta^2 - x'y^2}{\rho\zeta^3} \quad \left[\frac{\cos\phi}{\rho}\right].
\end{aligned} \tag{32}$$

The three components of the electric field follow from (11)

$$
\begin{aligned}
E_\rho(\mathbf{r},\mathbf{r}') &= \frac{p}{2\pi\sigma_0}\left(-\gamma_0^2\int_0^\infty \frac{h_\psi(z,z')}{k}\frac{1}{\rho}\partial^2_{\phi y}J_0(k\zeta)\,\mathrm{d}k + \int_0^\infty \frac{h_\pi^\dagger(z,z')}{k}\partial^2_{\rho x}J_0(k\zeta)\,\mathrm{d}k\right)\\
&\quad\left[\frac{p\cos\phi}{2\pi\sigma_0}\left(\frac{\gamma_0^2}{\rho}\int_0^\infty h_\psi(z,z')J_1(k\rho)\,\mathrm{d}k - \int_0^\infty h_\pi^\dagger(z,z')(kJ_0(k\rho)-J_1(k\rho)/\rho)\,\mathrm{d}k\right)\right]\\
E_\phi(\mathbf{r},\mathbf{r}') &= \frac{p}{2\pi\sigma_0}\left(\gamma_0^2\int_0^\infty \frac{h_\psi(z,z')}{k}\partial^2_{\rho y}J_0(k\zeta)\,\mathrm{d}k + \int_0^\infty \frac{h_\pi^\dagger(z,z')}{k}\frac{1}{\rho}\partial^2_{\phi x}J_0(k\zeta)\,\mathrm{d}k\right)\\
&\quad\left[\frac{p\sin\phi}{2\pi\sigma_0}\left(-\gamma_0^2\int_0^\infty h_\psi(z,z')(kJ_0(k\rho)-J_1(k\rho)/\rho)\,\mathrm{d}k + \frac{1}{\rho}\int_0^\infty h_\pi^\dagger(z,z')J_1(k\rho)\,\mathrm{d}k\right)\right]\\
E_z(\mathbf{r},\mathbf{r}') &= -\frac{p}{2\pi\sigma_0}\partial_x\zeta\int_0^\infty \partial_{z'}g_\pi(z,z')k^2J_1(k\zeta)\,\mathrm{d}k\quad\left[-\frac{p\cos\phi}{2\pi\sigma_0}\int_0^\infty \partial_{z'}g_\pi(z,z')k^2J_1(k\rho)\,\mathrm{d}k\right],
\end{aligned}
\tag{33}
$$

where $\gamma_0^2 = -\mathrm{i}\omega\mu\sigma_0$. The magnetic field components follow from (10)

$$
\begin{aligned}
B_\rho(\mathbf{r},\mathbf{r}') &= \frac{\mu p}{2\pi}\left(\int_0^\infty \frac{\partial_z h_\psi(z,z')}{k}\partial^2_{\rho y}J_0(k\zeta)\,\mathrm{d}k + \int_0^\infty \frac{\partial_{z'}h_\pi(z,z')}{k}\frac{1}{\rho}\,\partial^2_{\phi x}J_0(k\zeta)\,\mathrm{d}k\right)\\
&\quad\left[-\frac{\mu p\sin\phi}{2\pi}\left(\int_0^\infty \partial_z h_\psi(z,z')\,(kJ_0(k\rho)-J_1(k\rho)/\rho)\;\mathrm{d}k - \frac{1}{\rho}\int_0^\infty \partial_{z'}h_\pi(z,\,z')J_1(k\rho)\,\mathrm{d}k\right)\right]\\
B_\phi(\mathbf{r},\mathbf{r}') &= \frac{\mu p}{2\pi}\left(\int_0^\infty \frac{\partial_{z'}h_\psi(z,z')}{k}\frac{1}{\rho}\partial^2_{\phi y}J_0(k\zeta)\,\mathrm{d}k - \int_0^\infty \frac{\partial_{z'}h_\pi(z,z')}{k}\,\partial^2_{\rho x}J_0(k\zeta)\,\mathrm{d}k\right)\\
&\quad\left[-\frac{\mu p\cos\phi}{2\pi}\left(\frac{1}{\rho}\int_0^\infty \partial_z h_\psi(z,z')J_1(k\rho)\,\mathrm{d}k - \int_0^\infty \partial_{z'}h_\pi(z,z')\,(kJ_0(k\rho)-J_1(k\rho)/\rho)\;\mathrm{d}k\right)\right]\\
B_z(\mathbf{r},\mathbf{r}') &= -\frac{\mu p}{2\pi}\partial_y\zeta\int_0^\infty g_\psi(z,z')k^2J_1(k\zeta)\,\mathrm{d}k\quad\left[-\frac{\mu p\sin\phi}{2\pi}\int_0^\infty g_\psi(z,z')k^2J_1(k\rho)\,\mathrm{d}k\right].
\end{aligned}
\tag{34}
$$

For a centered source of finite length L, (33)–(34) must be numerically integrated from $x' = -L/2$ to $L/2$ after setting the source moment to $p = I\,\mathrm{d}x'$. The finiteness of the source is typically important only for observation points within a few times L of the dipole center, and the point source approximation given by the terms in square brackets in (33)–(34) is adequate at more distant locations.

Equations (33)–(34) may be simplified when the source dipole is of infinite extent. In the limit $L \to \infty$, all but the E_x, B_y and B_z components vanish, and the EM fields do not have any x dependence. The integrated Bessel function terms in (33)–(34) become

$$
\begin{aligned}
\int_{-\infty}^{\infty}\partial_x^2J_0(k\zeta)\,\mathrm{d}x' &= k\,(\pi k|y| - 2\cos(ky) - 2ky\,\mathrm{Si}(ky))\\
\int_{-\infty}^{\infty}\partial_y^2J_0(k\zeta)\,\mathrm{d}x' &= -k\,(\pi k|y| - 2ky\,\mathrm{Si}(ky)),
\end{aligned}
\tag{35}
$$

where $\mathrm{Si}(x)$ is the sine integral. The EM field components are given by

$$
\begin{aligned}
E_x\,(y,z,z') &= \frac{I}{2\pi\sigma_0}\left[\int_0^\infty \left(\gamma_0^2h_\psi(z,\,z') + h_\pi^\dagger(z,z')\right)(\pi k\,|y| - 2ky\,\mathrm{Si}\,(ky))\;\mathrm{d}k\;.\right.\\
&\quad\left. - 2\int_0^\infty h_\pi^\dagger(z,z')\;\cos(ky)\,\mathrm{d}k\right]\\
B_y\,(y,z,z') &= -\frac{\mu I}{2\pi}\left[\int_0^\infty \left(\partial_z h_\psi(z,z') + \partial_{z'}h_\pi(z,z')\right)(\pi k\,|y| - 2ky\,\mathrm{Si}(ky))\;\mathrm{d}k\right.\\
&\quad\left. - 2\int_0^\infty \partial_{z'}h_\pi(z,z')\;\cos(ky)\,\mathrm{d}k\right]\\
B_z\,(y,z,z') &= -\frac{\mu I}{2\pi}\int_0^\infty h_\psi(z,z')\,k\sin(ky)\,\mathrm{d}k.
\end{aligned}
\tag{36}
$$

The expression $\pi k|y| - 2ky\,\mathrm{Si}(ky)$ is a quasi-periodic (but asymptotically periodic) function of k, and is symmetric around $y = 0$. The field expressions may be evaluated numerically using a modification of the Chave (1983) Hankel transform algorithm in which $\pi k|y| - 2ky\,\mathrm{Si}(ky)$, $\sin(ky)$ and $\cos(ky)$ in (36) replace the Bessel function.

5 VERTICAL ELECTRIC DIPOLE SOURCE

The VED source was proposed by Edwards *et al.* (1981) for use in magnetometric surveying of the seafloor, and was subsequently applied to a number of geophysical targets. A VED couples to the seafloor approximately as the ratio of the seafloor to seawater conductivity as compared to the HED. Consequently, it does not provide high field penetration under the typical circumstance where the seafloor is more resistive than seawater.

Consider a point electric source dipole located at $(0, 0, z')$ and oriented in the $\hat{z}$ direction, so that $\mathbf{J}^0 = p\delta(x)\delta(y)\delta(z - z')\hat{z}$. It immediately follows that $\Upsilon = T = 0$, so that there is no PM mode. The TM mode scalar function is

$$\Pi(\mathbf{r}, z') = \frac{\mu p}{2\pi} \int_0^\infty g_\pi(z,z') k J_0(k\rho)\, \mathrm{d}k, \tag{37}$$

where $\langle \Pi \rangle = 0$; replacing g_π with h_π is unnecessary because $\int_0^\infty k J_0(k\rho)\, \mathrm{d}k = 0$. For a finite length source extending from $-H < a < b \leq 0$ with source moment $p = I\, \mathrm{d}z'$, the Green's function in (37) may be integrated to yield the closed form solution $G_\pi(z) = \int_a^b g_\pi(z,\ z')\, \mathrm{d}z'$. From symmetry considerations, the magnetic field is azimuthal about the source, whereas the electric field has only radial and vertical components, and the terms follow from (10) and (11)

$$\begin{aligned} B_\phi(\mathbf{r}) &= -\frac{\mu I}{2\pi} \int_0^\infty G_\pi(z)\, k^2 J_1(k\rho)\, \mathrm{d}k \\ E_\rho(\mathbf{r}) &= \frac{I}{2\pi\sigma_0} \int_0^\infty \partial_z G_\pi(z)\, k^2 J_1(k\rho)\, \mathrm{d}k \\ E_z(\mathbf{r}) &= -\frac{I}{2\pi\sigma_0} \int_0^\infty G_\pi(z)\, k^3 J_0(k\rho)\ \mathrm{d}k. \end{aligned} \tag{38}$$

6 VERTICAL MAGNETIC DIPOLE SOURCE

Coggon & Morrison (1970) presented a theoretical analysis of a VMD source near the seafloor. Cheesman *et al.* (1987) derived the transient response for a VMD, showing that it could be useful in the unusual instance where the subsurface target is more conductive than seawater. However, marine CSEM apparatus based on the VMD does not appear to have been developed.

Consider an infinitesimally thin loop of electric current of radius a and magnitude I oriented in the $x-y$ plane at a height z' (Fig. 2), so that the source electric current density is given by

$$\mathbf{J}^0(\mathbf{r}) = I\delta(\rho - a)\delta(z - z')\hat{\phi}, \tag{39}$$

where the sign has been chosen so that the magnetic moment points in the $\hat{z}$ direction. From (8), the consoidal part of the horizontal current vanishes, and because there is no vertical current source, there is no TM mode. The Fourier transform of (7) is

$$\tilde{\Upsilon}(z,\ z') = 2M \frac{J_1(ka)}{ka} \delta(z - z'), \tag{40}$$

where $M = I\pi a^2$ is the source magnetic dipole moment and $\langle \Upsilon \rangle = 0$. Substituting (40) into (19), applying the inverse Fourier transform (15) along with Poisson's formula (28) and verifying the zero average condition on Ψ yields

$$\Psi(\mathbf{r}, z') = \frac{\mu M}{\pi a} \int_0^\infty g_\psi(z, z') J_1(ka) J_0(k\rho)\, \mathrm{d}k. \tag{41}$$

By symmetry, the radial and vertical electric and azimuthal magnetic fields vanish. The remaining electric field component follows from (11)

$$E_\phi(\mathbf{r}, z') = \frac{i\omega\mu M}{\pi a} \int_0^\infty g_\psi(z,\ z') k J_1(ka) J_1(k\rho)\, \mathrm{d}k, \tag{42}$$

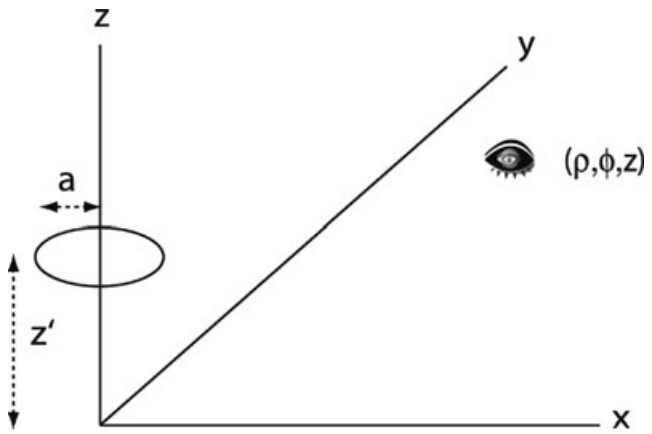

Figure 2. Diagram showing the geometry for a finite vertical magnetic dipole of radius a as described in the text. The loop source lies in the x–y plane at $(0, 0, z')$ with current flowing so that the magnetic moment points in the z-direction. The observation point at (ρ, ϕ, z) is depicted by the eye.

whereas the two magnetic field components obtain from (10)

$$B_\rho(\mathbf{r}, z') = -\frac{\mu M}{\pi a}\int_0^\infty \partial_z g_\psi(z,\, z')k\, J_1(ka).J_1(k\rho)\,\mathrm{d}k$$

$$B_z(\mathbf{r}, z') = \frac{\mu M}{\pi a}\int_0^\infty g_\psi(z,\, z')k^2\, J_1(ka).J_0(k\rho)\,\mathrm{d}k. \tag{43}$$

Eqs (42) and (43) are exact, and include the geometric effects of a finite current loop through the $J_1(ka)$ term. For points at horizontal distance $\rho \gg a$, the Bessel function $J_1(ka)$ may be approximated by the first term $ka/2$ in its series expansion. The resulting approximate forms of (42)–(43) are equivalent to those obtained by including point magnetic dipole sources in the pre-Maxwell equations. However, the full solutions (42)–(43) are easily evaluated numerically at horizontal ranges $\rho \gg a$ because $J_1(ka)$ changes very slowly compared to the range-dependent Bessel function term. Note further that (42)–(43) are well-defined at the center of the source loop, where $\rho = 0$.

7 HORIZONTAL MAGNETIC DIPOLE SOURCE

Dey & Ward (1970) derived the EM fields produced by an HMD source in air above a layered Earth. In this instance, no TM mode is induced in the ground, and the EM coupling becomes purely inductive. Cheesman *et al.* (1987) derived the EM fields for an oceanic HMD (which does induce a TM mode) with magnetic receivers, and a frequency domain HMD system is described by Evans (2007).

Consider an infinitesimally thin current loop of radius a and magnitude I oriented in the $x-z$ plane such that its magnetic moment points in the $\hat{y}$ direction (Fig. 3). The center of the loop is at (0, 0, a) where $-H + a \le z' \le -a$. An infinitesimal piece of the loop oriented at a clockwise angle α from the x-axis carries an electric current density

$$\mathrm{d}\mathbf{J}^0 = (I\alpha\,\mathrm{d}\alpha)\delta(x - a\cos\alpha)\delta(y)\delta(z - z' + a\sin\alpha)\,\hat{\alpha} \tag{44}$$

where $\hat{\alpha} = -\sin\alpha\hat{x} - \cos\alpha\hat{z}$. Integrating α over a complete circle yields the source current density

$$\mathbf{J}^0(\mathbf{r}, z') = -Ia\delta(y)\int_0^{2\pi}\delta(x - a\cos\alpha)\delta(z - z' + a\sin\alpha)(\sin\alpha\,\hat{x} + \cos\alpha\hat{z})\,\mathrm{d}\alpha. \tag{45}$$

Decomposing (45) using (6)–(8) and taking Fourier transforms gives

$$\tilde{\Upsilon} = \frac{\mathrm{i}\xi Ia}{k^2}\int_0^{2\pi}\mathrm{e}^{\mathrm{i}\eta a\cos\alpha}\delta(z - z' + a\sin\alpha)\sin\alpha\,\mathrm{d}\alpha$$

$$\tilde{T} = -\frac{\mathrm{i}\eta Ia}{k^2}\int_0^{2\pi}\mathrm{e}^{\mathrm{i}\eta a\cos\alpha}\delta(z - z' + a\sin\alpha)\sin\alpha\,\mathrm{d}\alpha$$

$$\tilde{\Xi} = -Ia\int_0^{2\pi}\mathrm{e}^{\mathrm{i}\eta a\cos\alpha}\delta(z - z' + a\sin\alpha)\sin\alpha\,\mathrm{d}\alpha, \tag{46}$$

yielding $\langle\Upsilon\rangle = \langle T\rangle = 0$ by inspection. Substituting into (19)–(20), taking the inverse Fourier transform (15) and applying Poisson's formula (28) gives

$$\Psi(\mathbf{r}, z') = -\frac{\mu M}{2\pi^2 a}\int_0^\infty\int_0^{2\pi}\frac{h_\psi\,(z, z' - a\sin\alpha)}{k}\,\partial_y J_0(k\zeta)\sin\alpha\,\mathrm{d}\alpha\,\mathrm{d}k \tag{47}$$

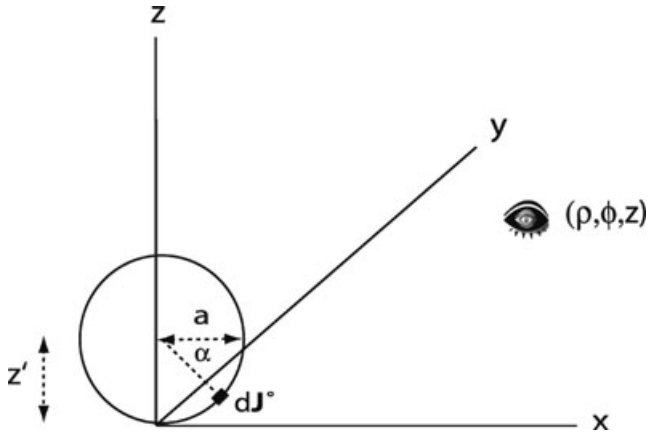

Figure 3. Diagram showing the geometry for a finite horizontal magnetic dipole of radius a as described in the text. The loop source lies in the x–z plane at (0, 0, z') with current flowing so that the magnetic moment points in the y-direction. The angle α used in the derivation is oriented clockwise from the x-axis. The observation point at (ρ, ϕ, z) is depicted by the eye.

$$\Pi(\mathbf{r}, z') = \frac{\mu M}{2\pi^2 a}\left[-\int_0^\infty \int_0^{2\pi} h_\psi(z, z' - a\sin\alpha)\, kJ_0(k\zeta)\cos\alpha \,\mathrm{d}\alpha \,\mathrm{d}k \right.$$
$$\left. + \int_0^\infty \int_0^{2\pi} \frac{\partial_{z'} h_\pi(z, z' - a\sin\alpha)}{k}\, \partial_x J_0(k\zeta)\sin\alpha \,\mathrm{d}\alpha \,\mathrm{d}k\right], \tag{48}$$

where $\zeta^2 = \rho^2 + a^2\cos^2\alpha - 2\,\rho\, a\cos\alpha\cos\phi$ and the zero average conditions on Ψ and Π have been satisfied. Eqs (47) and (48) are exact, and the EM fields may be computed by differentiation using (10) and (11) combined with a pair of numerical quadratures.

An approximate solution for an infinitesimal source where $a \to 0$ such that M remains fixed may be found by explicitly writing out the exponential terms in the Green's functions for points z above and below the loop, and considering the double Fourier transform form of (47)–(48) prior to applying Poisson's formula. Using the generating functions for regular and modified Bessel functions of the first kind

$$\mathrm{e}^{\mathrm{i}\eta a\cos\alpha} = J_0(\eta a) + 2\sum_{n=1}^{\infty} i^n J_n(\eta a)\cos(n\alpha)$$
$$\mathrm{e}^{\beta_0 a\sin\alpha} = I_0(\beta_0 a) + \sum_{n=1}^{\infty} I_n(\beta_0 a)\cos\left(n(\alpha - \pi/2)\right) \tag{49}$$

yields

$$\int_0^{2\pi} \mathrm{e}^{\mathrm{i}\eta a\cos\alpha}\mathrm{e}^{\beta_0 a\sin\alpha}\sin\alpha\,\mathrm{d}\alpha = 2\pi I_1(\beta_0 a)\, J_0(\eta a) + 2\pi\sum_{n=1}^{\infty} J_{2n}(\eta a)(I_{2n-1}(\beta_0 a) + I_{2n+1}(\beta_0 a))$$
$$\int_0^{2\pi} \mathrm{e}^{\mathrm{i}\eta a\cos\alpha}\mathrm{e}^{\beta_0 a\sin\alpha}\cos\alpha\,\mathrm{d}\alpha = 2\pi\sum_{n=1}^{\infty}(-1)^n i^{2n-1} J_{2n-1}(\eta a)(I_{2n}(\beta_0 a) - I_{2n-1}(\beta_0 a)). \tag{50}$$

For sufficiently small a, (50) reduces to $\pi\beta_0 a$ and $i\pi\eta a$, respectively. Writing out the terms in the Green's functions defined in (16) explicitly for $z > z' + a$ and $z < z' - a$ under this approximation, it can be shown that

$$\int_0^{2\pi} \frac{g_\psi(z, z' - a\sin\alpha)}{\pi a}\mathrm{e}^{\mathrm{i}\eta a\cos\alpha}\sin\alpha\,\mathrm{d}\alpha \approx -\partial_{z'} g_\psi(z, z')$$
$$\int_0^{2\pi} \frac{\partial_{z'} g_\pi(z, z' - a\sin\alpha)}{\pi a}\mathrm{e}^{\mathrm{i}\eta a\cos\alpha}\sin\alpha\,\mathrm{d}\alpha \approx -\beta_0^2 g_\pi(z, z') - \delta(z - z')$$
$$\int_0^{2\pi} \frac{g_\pi(z, z' - a\sin\alpha)}{\pi a}\mathrm{e}^{\mathrm{i}\eta a\cos\alpha}\cos\alpha\,\mathrm{d}\alpha \approx \mathrm{i}\eta g_\pi(z, z'). \tag{51}$$

whereas $T \approx 0$. The point source solutions for the PM and TM mode scalar functions are

$$\Psi\left(\mathbf{r}, z'\right) = \frac{\mu M}{2\pi}\int_0^\infty \frac{\partial_{z'} h_\psi(z, z')}{k}\partial_y J_0(k\rho)\,\mathrm{d}k \tag{52}$$

$$\Pi(\mathbf{r}, z') = -\frac{\gamma_0^2 \mu M}{2\pi}\int_0^\infty \frac{h_\pi(z, z')}{k}\partial_x J_0(k\rho)\,\mathrm{d}k. \tag{53}$$

The magnetic fields follow from (10)

$$B_\rho\left(\mathbf{r},\ z'\right) = -\frac{\mu\, M\sin\phi}{2\pi}\left[\int_0^\infty h_\psi^\dagger(z, z')\ (kJ_0\left(k\rho\right) - J_1(k\rho)/\rho)\ \mathrm{d}k - \frac{\gamma_0^2}{\rho}\int_0^\infty h_\pi(z, z')\, J_1(k\rho)\,\mathrm{d}k\right]$$
$$B_\phi\left(\mathbf{r},\ z'\right) = -\frac{\mu\, M\cos\phi}{2\pi}\left[\frac{1}{\rho}\int_0^\infty h_\psi^\dagger(z, z')\, J_1(k\rho)\,\mathrm{d}k - \gamma_0^2\int_0^\infty h_\pi(z, z')\,(kJ_0(k\rho) - J_1(k\rho)\,/\rho)\ \mathrm{d}k\right]$$
$$B_z\left(\mathbf{r},\ z'\right) = -\frac{\mu\, M\sin\phi}{2\pi}\int_0^\infty \partial_{z'} g_\psi(z, z')\, k^2 J_1(k\rho)\,\mathrm{d}k \tag{54}$$

and the electric fields obtain from (11)

$$E_\rho(\mathbf{r}, z') = -\frac{\mathrm{i}\omega\mu M\cos\phi}{2\pi}\left[\frac{1}{\rho}\int_0^\infty \partial_{z'} h_\psi(z, z')\, J_1(k\rho)\,\mathrm{d}k - \int_0^\infty \partial_z h_\pi(z, z')\,(kJ_0(k\rho) - J_1(k\rho)/\rho)\ \mathrm{d}k\right]$$
$$E_\phi(\mathbf{r}, z') = \frac{\mathrm{i}\omega\mu M\sin\phi}{2\pi}\left[\int_0^\infty \partial_{z'} h_\psi(z, z')\ (kJ_0(k\rho) - J_1(k\rho)/\rho)\,\mathrm{d}k - \frac{1}{\rho}\int_0^\infty \partial_z h_\pi(z, z')J_1(k\rho)\,\mathrm{d}k\right]$$
$$E_z(\mathbf{r}, z') = \frac{\mathrm{i}\omega\mu M\cos\phi}{2\pi}\int_0^\infty g_\pi(z, z')k^2 J_1(k\rho)\,\mathrm{d}k. \tag{55}$$

8 REPRESENTATION OF THE ELECTROMAGNETIC FIELD

In the absence of insight from ray concepts in diffusion physics, it is useful to examine the flow of energy to visualize CSEM field behaviour. Taking the dot product of **E** with (5), subtracting the dot product of **B** with (4) and using standard vector identities yields

$$\nabla\cdot\mathbf{S} + \partial_t w_B + \mathbf{J}\cdot\mathbf{E} = 0, \tag{56}$$

where $\mathbf{S} = (\mathbf{E} \times \mathbf{B})/\mu$ is the Poynting vector and $w_B = \boldsymbol{B} \cdot \boldsymbol{B}/2\mu$ is the internal energy in the magnetic field. There is no internal energy in the electric field under the pre-Maxwell approximation. A physical interpretation follows by applying the divergence theorem to (56). In a volume of material that does not include a source, **S** represents the amount of energy flowing into the volume per unit area per second that is balanced by thermodynamically irreversible Joule heating and the time rate of change of energy stored in the magnetic field within the volume.

For time harmonic fields, the terms in (56) may be represented as $\mathbf{E} = \mathrm{Re}(\boldsymbol{E}e^{-\mathrm{i}\omega t})$ and $\mathbf{B} = \mathrm{Re}(\boldsymbol{B}e^{-\mathrm{i}\omega t})$, where $\boldsymbol{E}$ and $\boldsymbol{B}$ are complex. It is easy to show that the Poynting vector is

$$\mathbf{S} = \frac{1}{2\mu}\left\{\mathrm{Re}\left(\boldsymbol{E} \times \boldsymbol{B}^*\right) + \mathrm{Re}\left[(\boldsymbol{E} \times \boldsymbol{B})\,\mathrm{e}^{-\mathrm{i}2\omega t}\right]\right\}, \tag{57}$$

where the superscript $(*)$ denotes the complex conjugate. The first term in (57) is real and time independent, whereas the second term is real and time-varying such that its time average is zero. Consequently, the time average of **S** is equal to the real part of the complex Poynting vector $\boldsymbol{S} = (\boldsymbol{E} \times \boldsymbol{B}^*)\,/\,2\mu$, where $\mathbf{S} \neq \boldsymbol{S}$. The real part of the complex Poynting vector represents the time-averaged energy flux into a volume of material that is balanced by Joule heating from (56).

The real part of the complex Poynting vector was used by Chave *et al.* (1990) to visualize the time-averaged energy flux for an earth model containing a low conductivity lithospheric zone bounded above and below by higher conductivity regions. Their results showed that the energy flux is large and nearly horizontal within the low conductivity region, with continuous leakage to the surface that produces a seafloor EM field that is enhanced over that which would be observed without the resistor. Weidelt (2007) presents analogous results for a hydrocarbon reservoir model. Similar behaviour will be seen for the reservoir models of Fig. 1, as further described in Sections 9–10.

The EM fields produced by controlled sources have a 3-D vector rather than a scalar form, and hence the standard practice of examining the amplitude and/or phase of Cartesian field components against range or frequency is not sufficient for understanding their behaviour. It is well known (e.g. Born & Wolf 2002, Section 1.4.3) that time harmonic vector fields can be depicted as a polarization ellipse oriented appropriately in space, and this representation serves as a complete description of the field. Further, the fact that an ellipse is required to represent the EM field indicates that its Cartesian components are not independent.

Let the equation for a time-harmonic ellipse be

$$\mathbf{e} = \left(ae^{i(\phi-\omega t)},\ ibe^{i(\phi-\omega t)}, 0\right)^T, \tag{58}$$

where $a \geq b \geq 0$. The parameters a and b are the lengths of the semi-major and semi-minor axes of the ellipse, respectively, and ϕ is the generalized phase. Eq. (58) represents counter-clockwise rotation as a function of time for a fixed value of ϕ. It can be converted to an ellipse arbitrarily oriented in space through three positive counter-clockwise rotations

$$\mathbf{R} = \begin{bmatrix} 1 & 0 & 0 \\ 0 & \cos\xi & \sin\xi \\ 0 & -\sin\xi & \cos\xi \end{bmatrix}, \tag{59}$$

where ξ is the roll around the semi-major (a) axis

$$\mathbf{P} = \begin{bmatrix} \cos\psi & 0 & \sin\psi \\ 0 & 1 & 0 \\ -\sin\psi & 0 & \cos\psi \end{bmatrix}, \tag{60}$$

where ψ is the pitch of the semi-major (a) axis and

$$\mathbf{S} = \begin{bmatrix} \cos\theta & \sin\theta & 0 \\ -\sin\theta & \cos\theta & 0 \\ 0 & 0 & 1 \end{bmatrix}, \tag{61}$$

where θ is the strike of the semi-major (a) axis. The electric or magnetic field at a given observation point may be written

$$\mathbf{E} = \mathbf{RPSe}. \tag{62}$$

After some tedious algebra, the six parameters representing the polarization ellipse are given by

$$a = \sqrt{\left(|\mathbf{E}\cdot\mathbf{E}^*|^2 + |\mathbf{E}\cdot\mathbf{E}|\right)/2}$$

$$b = \sqrt{\left(|\mathbf{E}\cdot\mathbf{E}^*|^2 - |\mathbf{E}\cdot\mathbf{E}|\right)/2}$$

$$\tan(2\phi) = \frac{\mathrm{Im}\ (\mathbf{E}\cdot\mathbf{E})}{\mathrm{Re}\ (\mathbf{E}\cdot\mathbf{E})}$$

$$\tan\theta = \frac{a\,\mathrm{Im}\left(E_\rho \mathrm{e}^{-i\phi}\right)}{b\,\mathrm{Re}\ \left(E_\rho \mathrm{e}^{-i\phi}\right)}$$

$$\tan\xi = \frac{\mathrm{Im}\left(E_z^* E_\rho\right)}{\mathrm{Im}\left(-E_\phi^* E_\rho\right)}$$

$$\tan\psi = -\frac{\mathrm{Im}\left(E_z^* E_\phi\right)}{\sqrt{\mathrm{Im}^2\left(E_z^* E_\rho\right) + \mathrm{Im}^2\left(E_\phi^* E_\rho\right)}}. \tag{63}$$

There is an inherent ambiguity in this representation, as (62) is unchanged if any pair of (θ, ϕ), (θ, ξ) and (ξ, ϕ) are altered by 180°. This can easily be fixed because all three variables should be continuous (modulo 360°) without discontinuities. An alternative parameter to the semi-minor axis b is the ellipticity b/a that lies between 0 for a line and 1 for a perfect circle.

9 UNIMODAL SOURCES: THE VED AND VMD

For all save the simplest earth models, numerical solution for the EM fields (33)–(34), (38), (42)–(43), and (54)–(55) is essential. This requires the computation of zero and first-order Hankel transforms. Throughout this paper, the direct numerical integration algorithm of Chave (1983) based on Gauss quadrature between the zero crossings of a Bessel function combined with Pade′ approximant convergence acceleration will be used. With the speed of modern computers, the computational overhead of direct numerical integration compared to digital filter algorithms is not a significant factor, whereas the accuracy advantage for more complicated models is important. In addition, the ability of the Pade′ approximant to correctly sum divergent series is essential when calculating the EM fields within the sub-seafloor structure.

The behaviour of CSEM fields is best understood in terms of the relevant distance scale governing the diffusion physics, the skin depth over which the EM field attenuates by 1/e. Throughout this paper, results for a 1 Hz source will be presented; this is in the middle of the practical frequency range of 0.1−10 Hz. At 1 Hz, a skin depth is 280 m in seawater, 710 m in the 0.5 S m^{-1} substrate (hereafter called the burial skin depth), 225 m in the 5 S m^{-1} brine layer, 2250 m in the 0.05 S m^{-1} weak hydrocarbon layer, and 3900 m in the 0.017 S m^{-1} strong hydrocarbon layer. Given that the physical distance scales in the reservoir model are 950 m (depth to the reservoir) and 100 m (thickness of the reservoir), it should be expected that the seafloor EM fields will be influenced to varying degrees by more than a single part of the structure at a given range, so that the diffusion physics governing CSEM fields is quite heterogeneous. In addition, the buried layer is electrically thin for all of the models, ranging from 0.4 skin depth for the brine reservoir to 0.03 skin depth for the strong hydrocarbon reservoir.

Fig. 4 (bottom panel) shows the radial electric field produced by a 1 Hz VED source for the brine, weak and strong hydrocarbon reservoirs in Fig. 1 and for an ocean of 5000 m depth. The water layer is about 18 skin depths thick, hence is nearly the same as an infinitely deep ocean. In each case, the electric field for the model with a reservoir is normalized to that for a 5000 m ocean overlying a uniform half-space of conductivity 0.5 S m^{-1} to remove the strong exponential fall-off of the field with range, facilitating interpretation. For this purely TM mode source, the brine reservoir model results in weak field enhancement above that for a half-space at short (∼1000–5000 m) ranges followed by attenuation at larger distances. In contrast, the hydrocarbon models display monotonic field enhancement with range, with the weak and strong reservoirs displaying an increase of about 6 and 100 at 10 000 m range, respectively.

Fig. 4 (middle and top panel) shows the radial and azimuthal TM mode fields at an azimuth of 0° and 90°, respectively, produced by a 1 Hz HED source. These two orientations are usually referred to as the in-line and parallel (or sometimes broadside) directions. In each case, the TM mode has been normalized by the corresponding component (TM + PM mode) for a half-space of conductivity 0.5 S m^{-1}. The in-line field (middle panel) is nearly identical to that produced by a VED (bottom panel) except very close to the source where direct diffusion through the ocean is dominant. In contrast, the parallel TM mode field (top panel) is weaker than the half-space field at all ranges for the brine reservoir, approaches the half-space value at a range of 10 000 m for the weak hydrocarbon reservoir model, and is larger than the half-space value at ranges over 4000 m for the strong reservoir model. Because the hydrocarbon reservoir TM mode normalized response increases monotonically with range, it follows that the presence of a thin resistive layer will always result in dominance of the measured EM field by the TM mode at a sufficient range in both the in-line and parallel configurations for an HED source.

Fig. 5 (bottom panel) shows the azimuthal electric field produced by a VMD source for the three reservoir models and normalized as in Fig. 4. For this purely PM mode source, the brine reservoir model produces rapid attenuation with range compared to a half-space to about 5000 m, after which it continues to decrease at a slower rate. In contrast, the PM mode response to the hydrocarbon reservoirs is nearly indistinguishable from that to a half-space, displaying only a miniscule increase with range that is nearly identical for the two models.

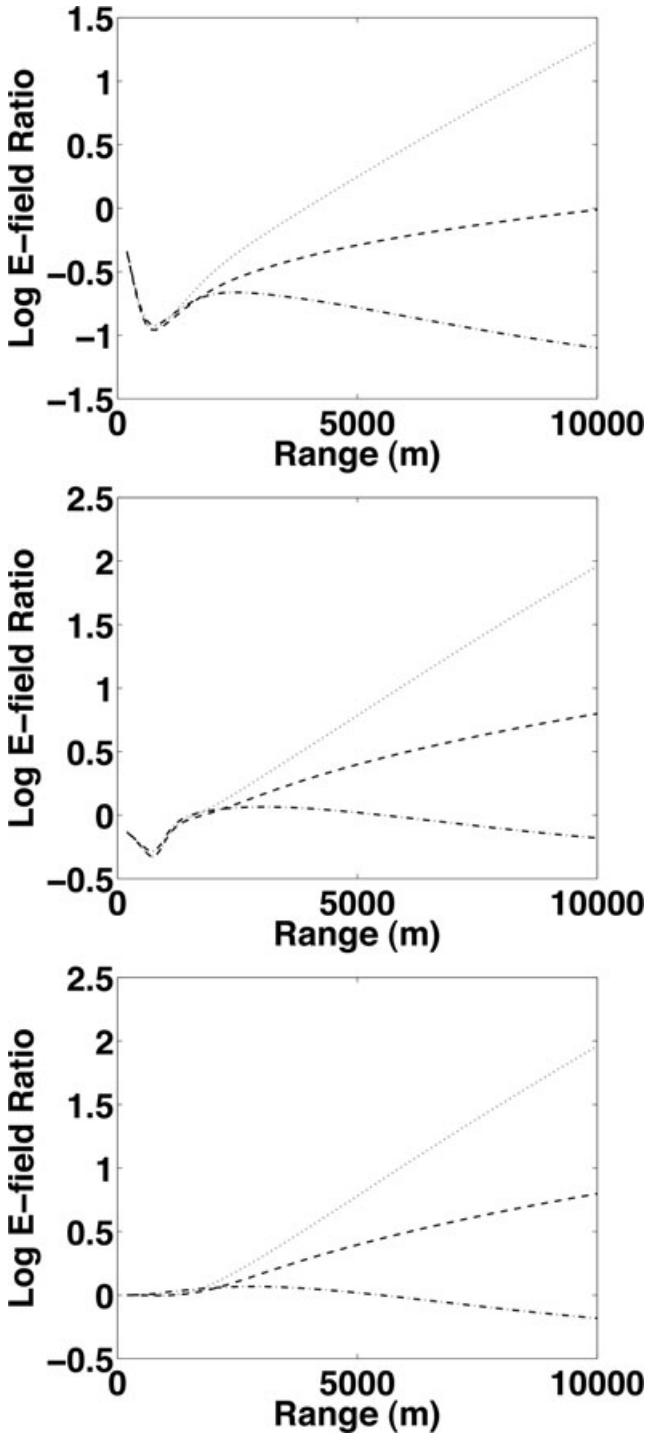

Figure 4. The logarithm of the normalized electric field amplitude on the seafloor as a function of source–receiver offset produced by a 1 Hz point source located 50 m above the seafloor at a range of 0. With reference to Fig. 1, the water depth H is 5000 m, the dot-dash line represents the brine reservoir, the dashed line represents the weak hydrocarbon reservoir, and the dotted line represents the strong hydrocarbon reservoir. The three panels show the radial electric field for a VED source (bottom), the radial TM mode electric field at an azimuth of 0° for an HED source (middle), and the azimuthal TM mode electric field at an azimuth of 90° for an HED source (top). The field for each model has been normalized to the same component of the electric field for a half-space of conductivity 0.5 S m^{-1}. For the HED source, this is the sum of the TM and PM modes.

Fig. 5 (middle and top panels) show the in-line and parallel PM mode fields for an HED source for the three reservoir models normalized as in Fig. 4. The parallel response (top panel) is nearly identical to that for a VMD, showing attenuation for the brine model and no effect for the two hydrocarbon models. The in-line response (middle panel) displays attenuation with range relative to the total field in the in-line direction for all reservoir models, although the effect is more pronounced for brine.

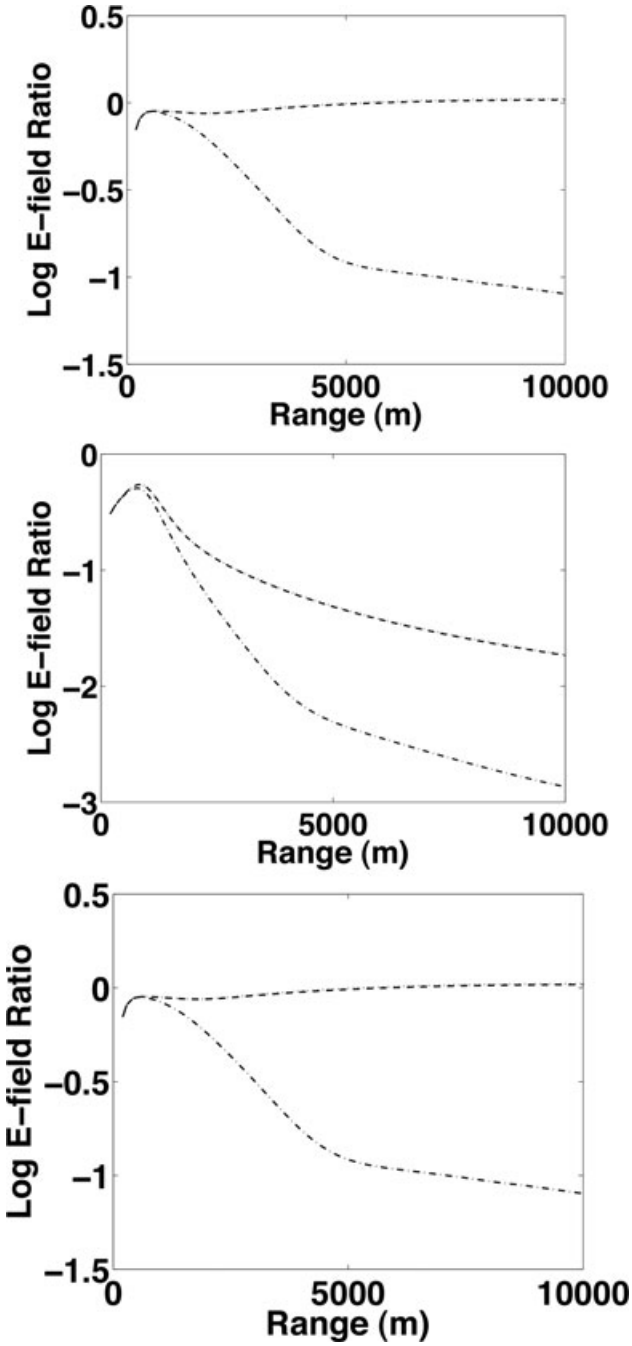

Figure 5. The logarithm of the normalized electric field amplitude on the seafloor as a function of source–receiver offset produced by a 1 Hz point source located 50 m above the seafloor at a range of 0. With reference to Fig. 1, the water depth H is 5000 m, the dot-dash line represents the brine reservoir, the dashed line represents the weak hydrocarbon reservoir, and the dotted line represents the strong hydrocarbon reservoir. The two hydrocarbon models produce nearly identical responses, and are nearly superimposed in the diagram. The three panels show the azimuthal electric field for a VMD source (bottom), the radial PM mode electric field at an azimuth of 0° for an HED source (middle), and the azimuthal PM mode electric field at an azimuth of 90° for an HED source (top). The field for each model has been normalized to the same component of the electric field for a half-space of conductivity 0.5 S m^{-1}. For the HED source, this is the sum of the TM and PM modes.

Because the HED models in Figs 4 and 5 have been normalized by the same total half-space electric field, the relative size of the TM and PM modes may be directly compared. For the in-line configuration, the TM mode dominates the PM mode at ranges beyond about 1000 m (or four seawater skin depths) independent of the underlying resistivity structure. This observation extends to a half-space. The relative size of the modes becomes larger in the presence of an increasingly resistive sub-surface structure. For the parallel configuration over a brine reservoir, the PM mode is larger than the TM mode only at ranges under about 3500 m and is of comparable size at longer ranges. For the parallel configuration over a hydrocarbon reservoir, the PM mode is larger than the TM mode at short ranges, but there always exists a range beyond which the TM mode becomes increasingly dominant. For the weak reservoir model, this occurs at about 12 000 m, whereas for the

strong reservoir model, it happens at about 4000 m. For a half-space model, the PM mode is always larger than the TM mode in the parallel direction. In all instances, the in-line total (TM + PM) electric field is substantially larger at all ranges as compared to the parallel direction.

All CSEM source types excite both electric and magnetic fields, and hence it might be expected that additional information will ensue from measuring all possible components. However, plots for the magnetic field such as Figs 4 and 5 are nearly identical in form to those for the electric field. In addition, plots of the ratio of the electric to the magnetic field as a function of range are nearly flat beyond 2000 m range. These observations suggest that there is limited additional information in the magnetic field, and hence in the absence of signal-to-noise considerations, little is gained beyond redundancy by measuring both the electric and magnetic fields. This is not meant to imply that for all source–receiver orientations, measurement of the electric and magnetic fields yields identical information about subsurface; in particular, the in-line and parallel geometries show a large difference. Finally, the HMD produces both TM and PM modes, and its response to the three reservoir models is identical in form to that for the HED beyond a range of a few skin depths in seawater where the source geometry induces differences within the ocean layer.

Frequency domain CSEM fields possess a phase (not shown) as well as a magnitude, and the observable electric field components are the sum of its complex TM and PM mode elements. It is well known that the phase changes at about one radian per skin depth in the part of the structure whose effect is dominant at a given range. In the presence of a resistive reservoir layer, the rate of the phase change with range decreases as the reservoir conductivity decreases. Examination of the phase of the two modes unsurprisingly shows that this effect is confined to the TM mode, with the PM mode phase nearly unchanged from that for a half-space. In the presence of a conductive reservoir, the roles of the two modes are reversed, although the effect of a conductor on the PM mode is weaker than that of a resistor on the TM mode for a given reservoir conductivity contrast.

Figs 6–10 extend the seafloor EM fields shown in Figs 4–5 to the entire electrical structure through visualization of the time-averaged energy flow via the Poynting vector representation in (56)–(57). The greyscale contours in Figs 6 and 9 represent the magnitude of the real

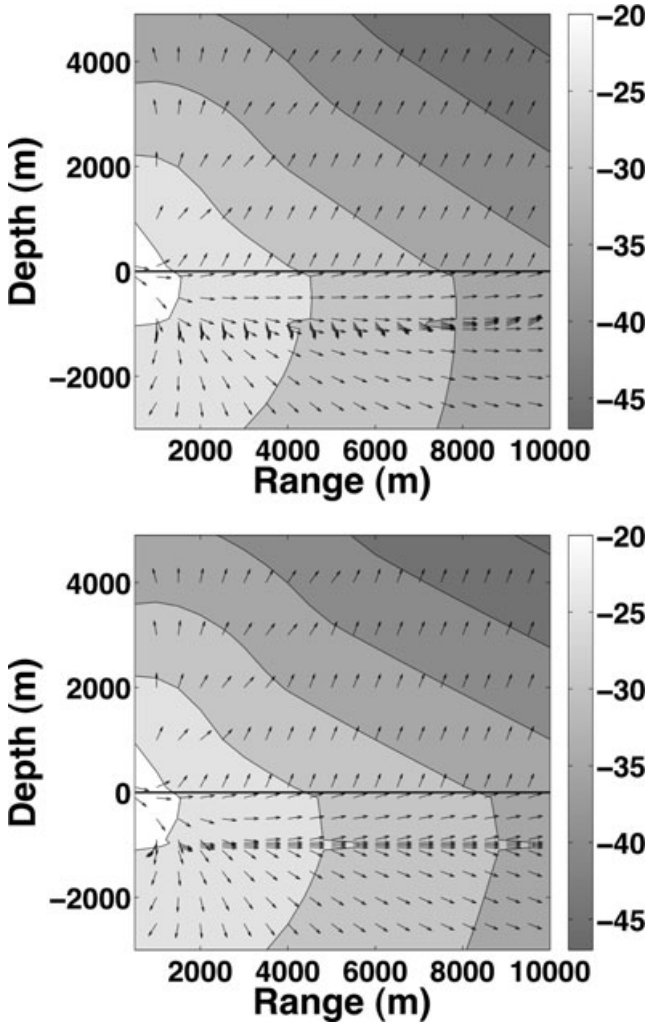

Figure 6. Contours of the logarithm of the magnitude of the real part of the complex Poynting vector (greyscale) and its local direction at the origin of each black arrow produced by a 1 Hz point VED source located 50 m above the seafloor at a range of zero. The arrow orientation has been adjusted for the different horizontal and vertical scales, and the black horizontal line depicts the seafloor. With reference to Fig. 1, the water depth H is 5000 m, the upper panel represents the brine reservoir and the lower panel represents the weak hydrocarbon reservoir.

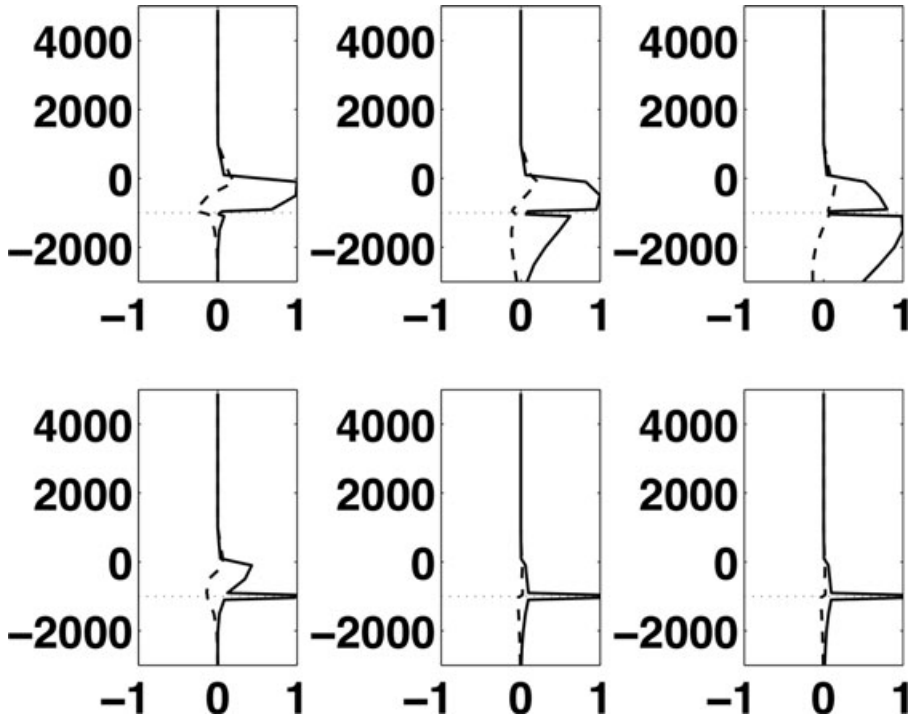

Figure 7. Vertical cuts through the brine and weak hydrocarbon models of Fig. 6 (top and bottom plots, respectively) showing the radial (solid) and vertical (dashed) components of the Poynting vector at ranges of 2000 m (left), 6000 m (middle) and 10 000 m (right). Each set of curves has been normalized to the maximum value at the given range. The weak dotted line indicates the center of the reservoir layer.

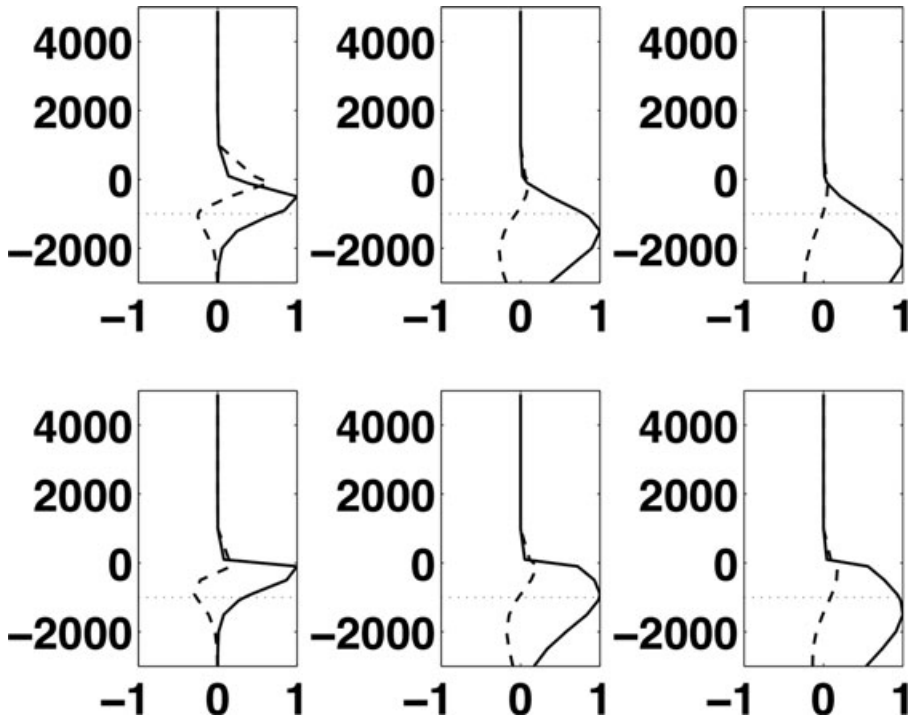

Figure 8. Vertical cuts through a uniform half-space of conductivity 0.5 S m^{-1} for a VMD (top panels) and VED (bottom panels) showing the radial (solid) and vertical (dashed) components of the Poynting vector at ranges of 2000 m (left), 6000 m (middle) and 10 000 m (right). Each set of curves has been normalized to the maximum value at the given range. The weak dotted line indicates the center of the 1000 m reservoir layer for reference.

part of the complex Poynting vector, whereas the black arrows show its direction at the arrow origin. Figs 7 and 10 show vertical cuts through the structure at three ranges.

Fig. 6 depicts the Poynting vector for a 1 Hz VED source (hence a purely TM mode) for the brine and weak hydrocarbon models. In each instance, the reservoir layer at 1000 m depth is represented by three closely spaced arrows at its center and 10 m inside its edges, and

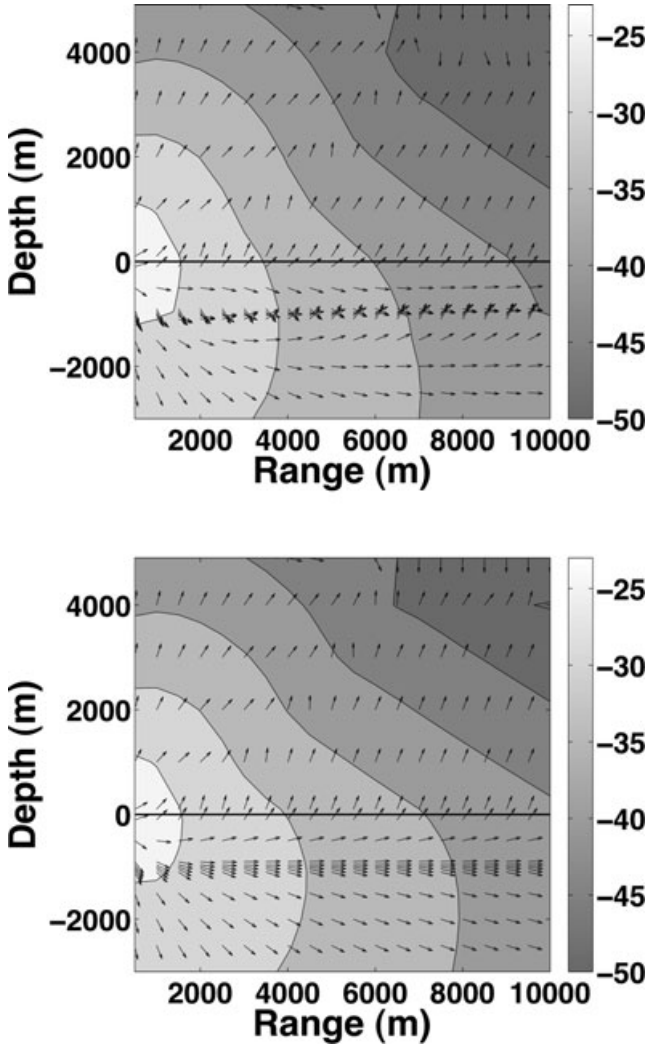

Figure 9. Contours of the logarithm of the magnitude of the real part of the complex Poynting vector (greyscale) and its local direction at the origin of each black arrow produced by a 1 Hz point VMD source located 50 m above the seafloor at a range of 0. The arrow orientation has been adjusted for the different horizontal and vertical scales, and the horizontal black line depicts the seafloor. With reference to Fig. 1, the water depth H is 5000 m, the upper panel represents the brine reservoir and the lower panel represents the weak hydrocarbon reservoir.

is bounded by arrows 100 m above and below the layer. For both models, energy flow in the ocean is upward and outward relative to the seafloor at ranges beyond 1000 m (or about 4 skin depths in seawater). At this distance, direct diffusion through seawater from the source is sufficiently weak that the EM field is dominated by the effect of diffusion through the sub-seafloor structure, as modified by the reservoir layer to produce the changes in the seafloor EM field depicted in Fig. 4 (bottom).

Fig. 6 (bottom) shows the Poynting vector for the weak hydrocarbon model. Guided energy flow within the reservoir is manifest as strong deflection of the Poynting vector magnitude contours away from the source and a nearly horizontal flow direction beyond a range of about 1500 m. This distance is the same for the strong reservoir model (not shown), hence does not depend on the reservoir conductivity. In fact, it corresponds to about 2 burial skin depths, illustrating the well-known (e.g. Chave & Cox 1982; Srnka 1986; Chave *et al.* 1991) rule of thumb that the source–receiver offset needs to be over 2−3 burial skin depths to detect a resistive layer. Energy flow in the overburden rotates from being downward and outward to horizontal to upward and outward between 2000 and 4000 m range, and thereafter is in a steady directional state. For increasing range, the Poynting vector magnitude at the seafloor for the hydrocarbon model is increasingly larger than that for the brine model at a given range, as is evident by comparing the top and bottom panels in Fig. 6. Overall, the behaviour of TM mode energy flow in the presence of a thin resistive layer is one of guided diffusion with continuous leakage into the over and underburden where dissipation is larger.

Enhanced Joule heating in the brine reservoir (top panel) is evident through the deflection of the Poynting vector magnitude contours toward the source within the reservoir layer. In addition, the energy flux is predominantly vertical downward within the brine layer near the source, becoming more horizontal with range until the flux is upward beyond about 8000 m. Concomitantly, the energy flux becomes nearly horizontal on either side of the layer, becoming somewhat more vertical with distance away from it. From Fig. 4 (bottom), the electric field is weakly enhanced over that for a half-space in the 1000–5000 m interval, corresponding to the range span where the energy flux in the upper

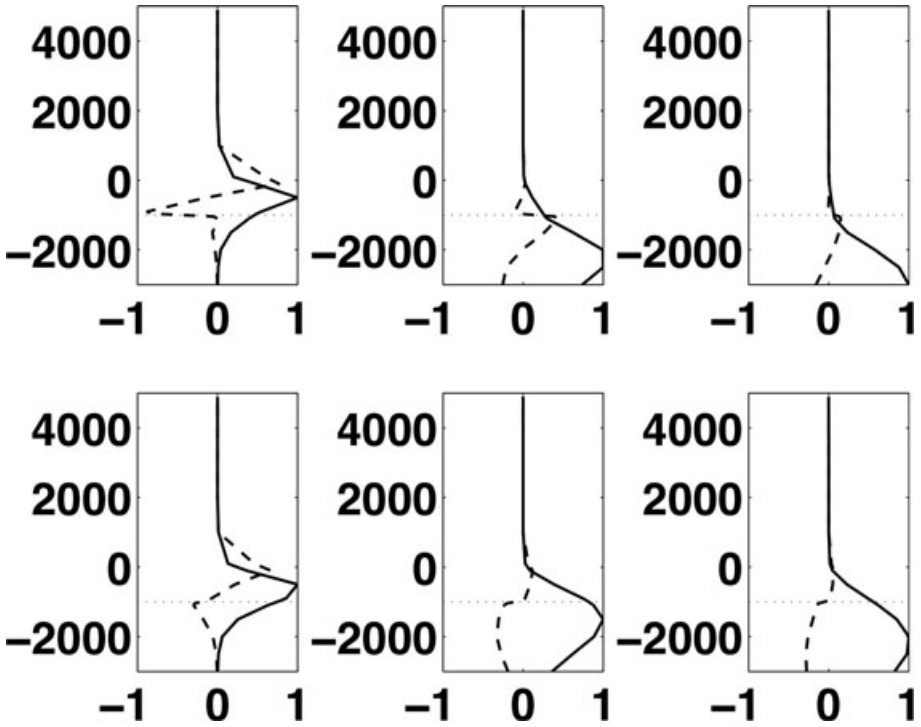

Figure 10. Vertical cuts through the brine and weak hydrocarbon models of Fig. 9 (top and bottom plots, respectively) showing the radial (solid) and vertical (dashed) components of the Poynting vector at ranges of 2000 m (left), 6000 m (middle) and 10 000 m (right). Each set of curves has been normalized to the maximum value at the given range. The weak dotted line indicates the center of the reservoir layer.

950 m in the Earth is the most horizontal, suggesting that the relatively resistive zone between the brine reservoir and seawater supports weak guided energy flow.

Fig. 7 shows vertical cuts of the VED Poynting vector at 2000, 6000 and 10 000 m range for the brine (top panels) and weak hydrocarbon (bottom panels) reservoirs. The bottom panels reinforce the conclusions from Fig. 6 (bottom): TM mode energy flow in the presence of a thin resistive layer is dominated by guided diffusion through it, and this characteristic is established within a few burial skin depths of the source. Further, the flow is weakly upward above and weakly downward below the layer beyond about 3000 m (or four burial skin depths). For the brine model, the reservoir is a locus of dissipation and not horizontal energy flow, as manifest by a minimum value for the Poynting vector within the layer. Further, the depth and vertical extent of peak horizontal energy flow moves deeper with range, consistent with the purely diffusional nature of marine CSEM.

Fig. 8 (bottom) provides an instructive comparison with Fig. 7 by showing vertical cuts of the VED Poynting vector for a half-space at the same ranges. For the hydrocarbon model, guided diffusion in the reservoir dominates over any tendency toward a half-space Poynting vector. For the brine reservoir model, there is close resemblance to the half-space Poynting vector except within the conductive layer. The presence of a conductive zone does not alter the range at which penetration of the peak energy flux reaches a given depth. Further, the increase of depth and breadth of the radial Poynting vector peak with range is consistent with a diffusion process.

Fig. 9 shows the Poynting vector cross-section for a 1 Hz VMD source (hence a purely PM mode) for the brine and weak hydrocarbon models. For both models and as for the TM mode in Fig. 6, energy flow in the ocean is upward and outward relative to the seafloor at ranges beyond a few skin depths in seawater. However, energy flux downward from the sea surface is increasingly evident beyond 5000 m range. This is due to a weak so-called air wave propagating along the seawater-air interface. Because a 5000 m ocean is electrically thick, the airwave is not strong enough to overcome the upward energy flux from the seafloor over the ranges depicted. However, at a sufficiently large range, the latter will attenuate such that the air wave will dominate the physics regardless of the subsurface structure, although this may well occur at ranges below the receiver noise floor in deep water.

Fig. 9 (bottom) depicts the Poynting vector for the weak reservoir model, and is nearly indistinguishable from the response to a uniform half-space. This is not unexpected because the purely inductive physics of the PM mode will easily couple across an electrically thin, resistive layer, and is consistent with the flat nature of the normalized electric field at the seafloor for both reservoir models in Fig. 5 (bottom).

Fig. 9 (top) depicts the Poynting vector for the brine reservoir model. In and immediately around the brine layer, the energy flux is downward from the source to about 1500 m (or 2 burial skin depths) range, and thereafter becomes downward above and in the upper parts of the reservoir and upward below and in the lower parts of the reservoir. The upward flow from below becomes more vertical whereas the downward flow from above becomes more horizontal with range. Concomitantly, the flow in the overburden changes from horizontal to downward and then back to being horizontal with a slight upward bias, whereas the flow in the underburden changes from downward to horizontal to upward. Further, the Poynting vector magnitude at the seafloor for a given range is consistently weaker for the brine as compared

to the hydrocarbon reservoir, whereas there is a decrease across the brine reservoir whose size increases with range. Taken together, these observations are consistent with a conductive reservoir acting as a locus for dissipation with no evidence for guided diffusion. The changing direction of energy flow reflects the complex interplay between the EM fields throughout the structure.

Fig. 10 shows vertical cuts of the radial and vertical VMD Poynting vector at the same ranges as for Fig. 7. For the resistive reservoir model (bottom), these are essentially the same as the half-space plots in Fig. 8 (top). For the brine reservoir in Fig. 10 (top), the presence of a conductor consistently acts to increase the depth of the peak radial energy flux at a given range as compared to a half-space. It also reverses the direction of the vertical Poynting vector across the conductive layer depth as compared to a half-space. Finally, for a given range, Fig. 10 suggests that the peak radial energy flux occurs at a larger depth for a PM mode as compared to a TM mode, an effect that is accentuated by the presence of a conductive zone, as seen by comparing Fig. 7 (top) with Fig. 10 (top).

Fig. 11 shows the Poynting vector for a 1 Hz VMD (bottom) and VED (top) for a 500 m deep ocean overlying a uniform half-space of conductivity 0.5 S m^{-1}. The results graphically illustrate a key difference between the PM and TM modes. The horizontal magnetic field for the latter vanishes at an interface with an insulator such as air, and hence the Poynting vector vanishes at the ocean-air boundary. As a result, the TM mode is not affected by an air wave. In contrast, the PM mode seafloor response is dominated by energy flow downward from the sea surface at ranges beyond about 4000 m, and the energy flux is increasingly downward throughout the subsurface structure as range increases.

Weidelt (2007) presents an elegant derivation of the functional form of the leading term for an HED air wave, and shows that its subtraction results in an EM field as a function of range that is largely the effect of subsurface structure. Although this is an important elucidation of the relevant physics, it is unlikely to be useful in practice, as it involves subtraction of two large quantities (the measured field and the analytic air wave formula) to reveal a much smaller one (the corrected field). As a result, small errors in the correction can produce

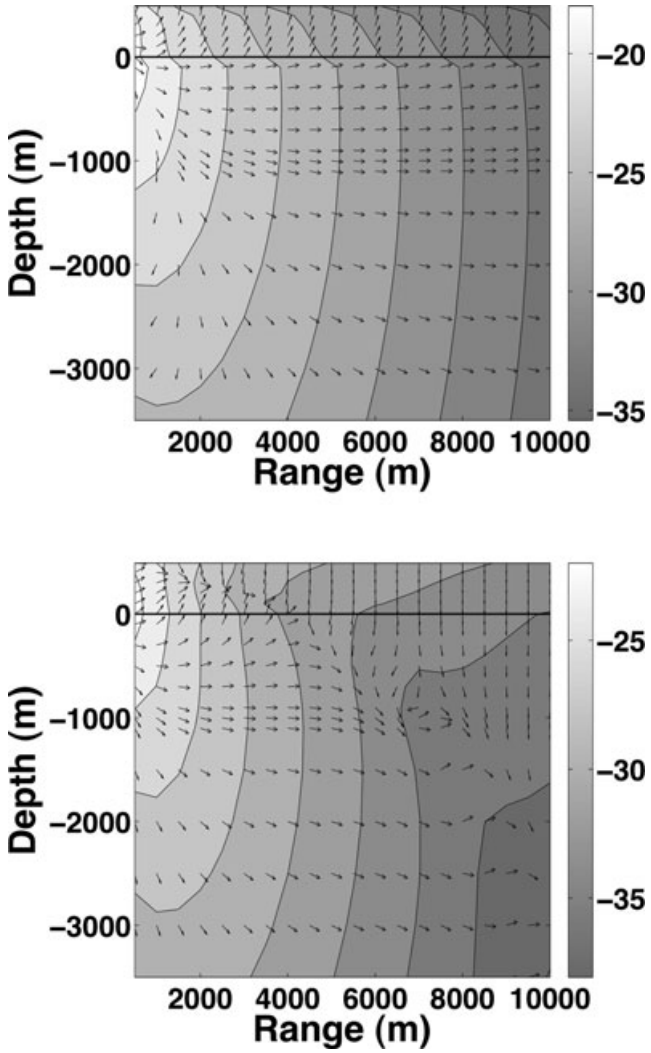

Figure 11. Contours of the logarithm of the magnitude of the real part of the complex Poynting vector (greyscale) and its local direction at the origin of each black arrow produced by a 1 Hz point VMD (bottom) and VED (top) source located 50 m above the seafloor at a range of 0. The arrow orientation has been adjusted for the different horizontal and vertical scales, and the horizontal black line depicts the seafloor. The water depth H is 500 m, and the subsurface electrical structure is a half-space ($\sigma = 0.5$ S m^{-1}).

large errors in the corrected field. Probably a more viable way to eliminate airwave effects is use of a time- rather than a frequency-domain approach, as has been suggested by others (e.g. Weiss 2007)

10 BIMODAL SOURCES: THE HED AND HMD

In contrast to the VED and VMD, horizontal electric and magnetic sources produce a mixture of TM and PM mode EM fields. At a given azimuth, the EM field can be represented as radial, azimuthal and vertical components that are interdependent. For simplicity, the present focus will be on the in-line and parallel directions. However, the electric field polarization ellipse becomes degenerate in these instances, reducing to an ellipse with a fixed strike of 0°, roll of 90° and pitch of 0° or a line, respectively. To more fully understand the behaviour of the triaxial electric field, it will be examined at azimuths of 5° and 85° prior to viewing the Poynting vector in the nearly equivalent in-line and parallel directions. Finally, the Poynting vector is the cross product of the electric and magnetic fields, so cannot be separated into distinct modal contributions for horizontal sources.

Fig. 12 shows the six ellipse parameters defined in (63) for the electric field produced by an HED source in a 5000 m deep ocean at an azimuth of 5°. Both the magnitude of the semi-major axis and the generalized phase are consistent with the discussion in Section 9, displaying electric field enhancement and a decrease in the phase slope with range as the conductivity of the reservoir layer decreases and a much weaker effect for a conductive reservoir. The ellipticity approaches 0.35 near the source where direct diffusion in seawater is dominant, and then becomes quite small. Beyond 4000 m, the semi-minor axis is about 1/20 of the semi-major axis for the hydrocarbon reservoir models, and

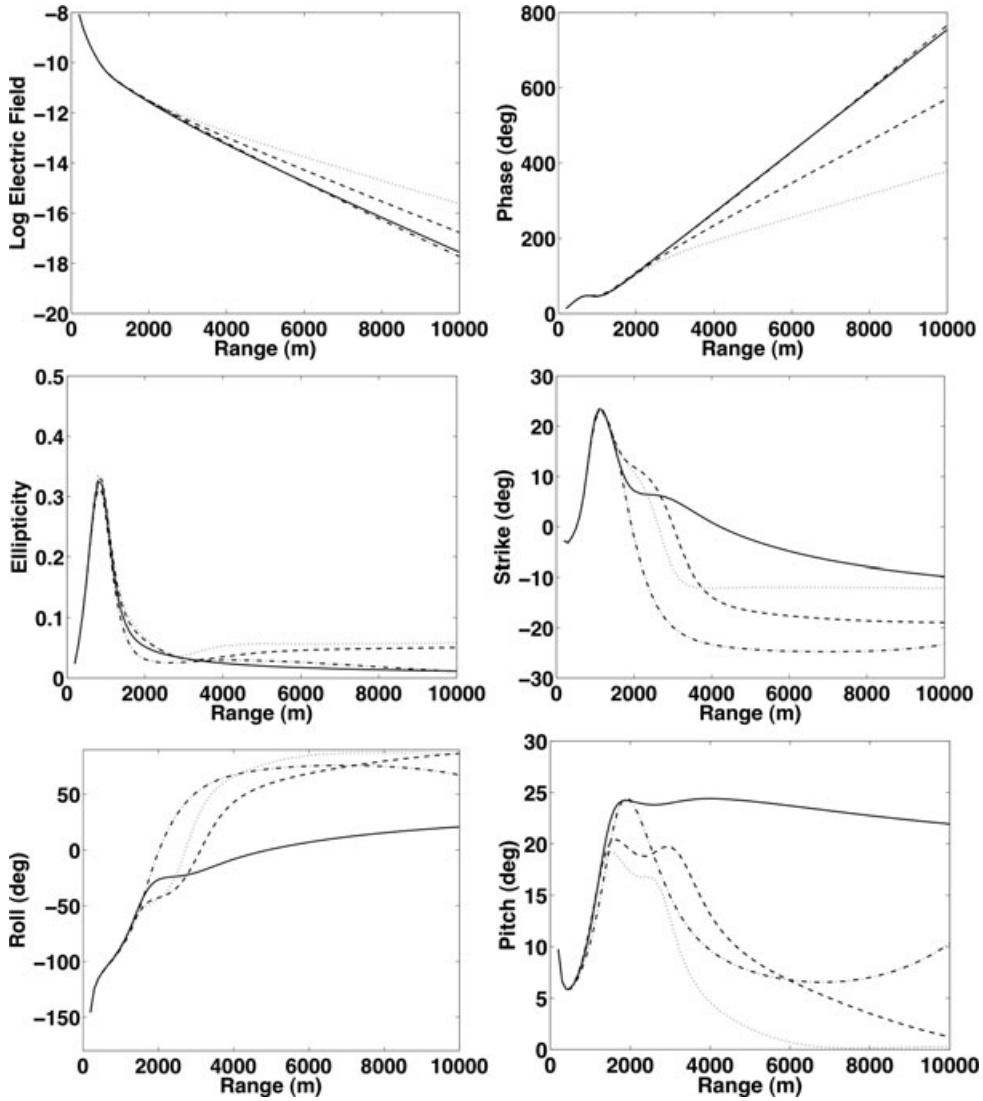

Figure 12. The six polarization ellipse parameters in (62)–(63) as a function of range for the 1 Hz seafloor electric field at an azimuth of 5° from a unit point HED source located 50 m above the seafloor at the origin. With reference to Fig. 1, the water depth H is 5000 m, the solid line represents a uniform half-space ($\sigma = 0.5$ S m^{-1}), the dot-dash line represents the brine reservoir, the dashed line represents the weak hydrocarbon reservoir, and the dotted line represents the strong hydrocarbon reservoir.

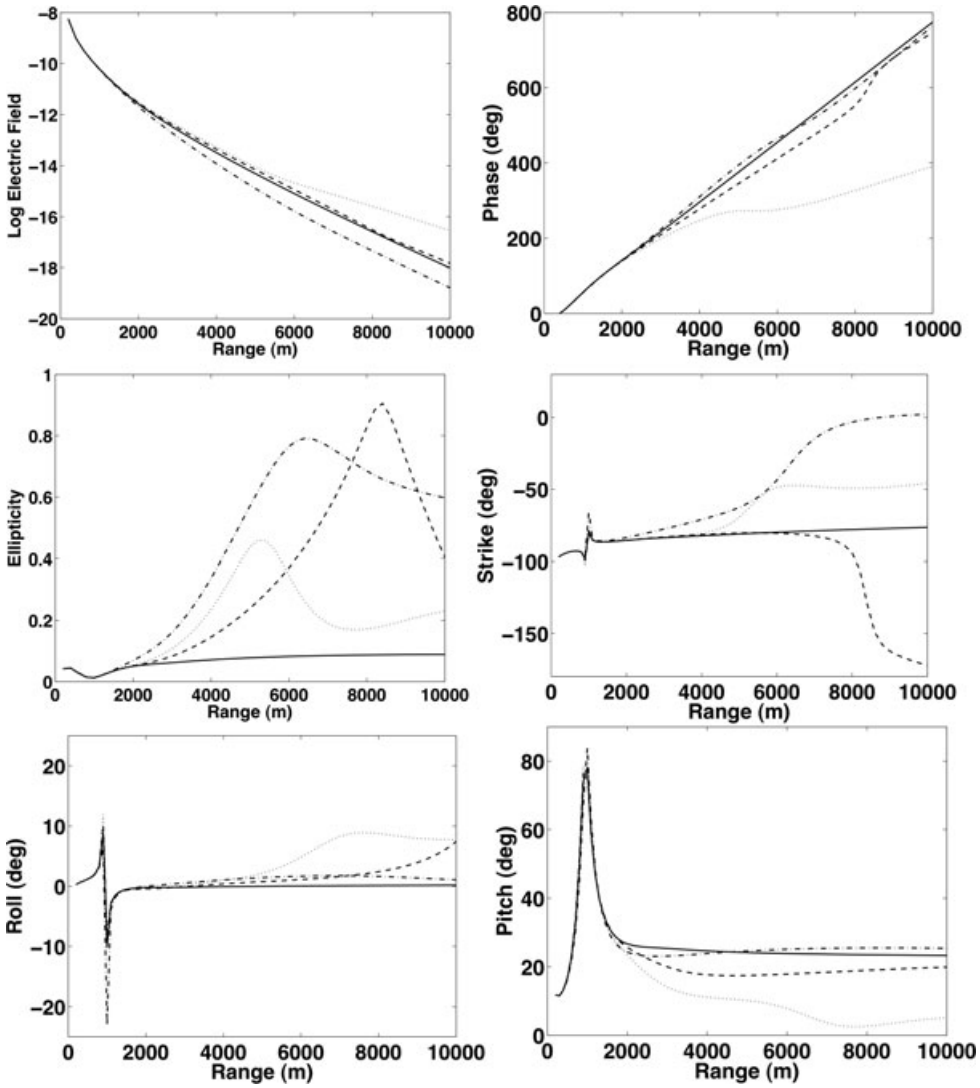

Figure 13. The six polarization ellipse parameters of (62)–(63) as a function of range for the 1 Hz seafloor electric field at an azimuth of 85° from a unit point HED source located 50 m above the seafloor at the origin. In all cases and with reference to Fig. 1, the water depth H is 5000 m, the solid line represents a uniform half-space ($\sigma = 0.5$ S m^{-1}), the dot-dash line represents the brine reservoir, the dashed line represents the weak hydrocarbon reservoir and the dotted line represents the strong hydrocarbon reservoir.

is even smaller for the half-space and brine models. The remaining three angle parameters show the largest variation as direct diffusion in seawater is overcome by diffusion through the subsurface. In particular, the roll indicates a change in the sense of rotation from clockwise to counter-clockwise during this transition. Systematic differences that depend on subsurface structure are also evident. Because the TM mode always dominates the PM mode in the in-line configuration, the variability evident in Fig. 12 is largely due to the former.

Fig. 13 shows the ellipse parameters for the electric field produced by an HED source in a 5000 m deep ocean at an azimuth of 85°. The magnitude is consistent with the discussion in Section 9, showing attenuation for a brine layer, a small difference from a half-space over the depicted ranges for a weak hydrocarbon reservoir and a substantial increase with range for a strong hydrocarbon reservoir. The generalized phase displays more structure than at 5° azimuth, with the hydrocarbon models peaking, then dipping and finally rising at a faster rate with range. The peak occurs at about 4000 and 8000 m range for the strong and weak hydrocarbon models, respectively, which are both smaller than the range where the amplitude changes. Concomitantly, the ellipticity peaks at values that approach circularity and the ellipse strike shifts dramatically, with weaker changes in the roll and pitch. The brine model also displays a marked change in ellipticity and strike, although with a different pattern.

Fig. 14 shows the ellipse parameters for the electric field produced by an HED source in a 1000 m deep ocean at an azimuth of 5°. For this water depth, the air wave effect is expected to be large, and is manifest as the well known flattening of the amplitude and phase curves at ranges where the upward diffusing electric field from below the seafloor becomes substantially weaker than the downward diffusing air wave that has a nearly constant amplitude and phase, reflecting the negligible fraction of a free space wavelength that 10 000 m range represents. Because the upward diffusing electric field is weaker for the half-space and brine models, this occurs at a smaller range compared to the weak reservoir model; the strong reservoir model does not show any perceptible effect in the amplitude and phase. However, comparison of

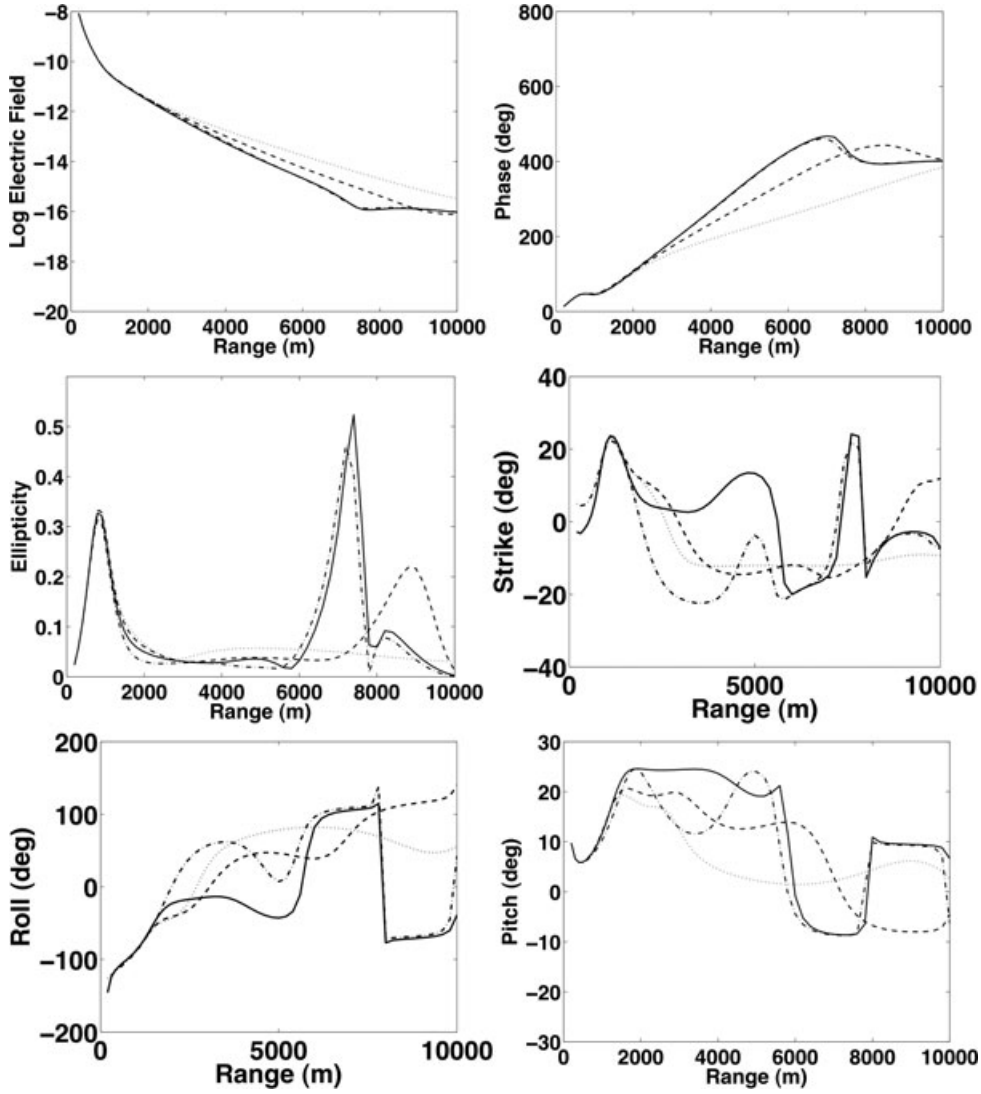

Figure 14. The six polarization ellipse parameters of (62)–(63) as a function of range for the 1 Hz seafloor electric field at an azimuth of 5° from a unit point HED source located 50 m above the seafloor at the origin. In all cases and with reference to Fig. 1, the water depth H is 1000 m, the solid line represents a uniform half-space ($\sigma = 0.5$ S m^{-1}), the dot-dash line represents the brine reservoir, the dashed line represents the weak hydrocarbon reservoir and the dotted line represents the strong hydrocarbon reservoir.

Figs 12 and 14 shows marked variability in the remaining ellipse parameters at smaller source–receiver offsets than for the amplitude and phase, including for the strong reservoir model.

By comparing Figs 12 and 13, it is apparent that sensitivity to resistive layers is higher at azimuths near the in-line orientation for an HED source, whereas sensitivity to conductive layers is more substantial at azimuths near the parallel one. However, this does not mean that measurement of the in-line orientation is always preferred in hydrocarbon applications. Constable & Weiss (2006) utilized synthetic inversions to show that the combination of the in-line and parallel orientations is required to resolve a resistive layer, and that use of only the in-line orientation misses the layer completely. Thus, measurement of the EM field over a range of azimuths is essential, as will inevitably happen in a practical survey.

Taken in aggregate, Figs 12–14 demonstrate that measurement of the triaxial rather than only the horizontal electric field components can yield additional information about subsurface structure. Similar results are obtained for the magnetic field. However, these diagrams do not provide great insight into the physics governing EM diffusion within the substrate, and hence it becomes necessary to investigate the Poynting vector.

Fig. 15 shows the Poynting vector for a 1 Hz HED source and the brine model in the in-line (bottom) and parallel (top) orientations. Because the TM mode always dominates the seafloor electric field in the in-line direction, it is expected that the corresponding HED Poynting vector will closely resemble that for a VED source. Comparison of Fig. 6 (top) and Fig. 15 (bottom) shows that this is indeed the case except for an increase in magnitude at a given range and a weak airwave near the sea surface for the HED. Vertical cuts through the cross-section closely resemble those in Fig. 7 (top). In contrast, the parallel seafloor electric field for a brine reservoir is largely PM mode at ranges under 3500 m (or 5 burial skin depths), and thereafter is a combination of TM and PM modes with comparable magnitudes out to the largest range

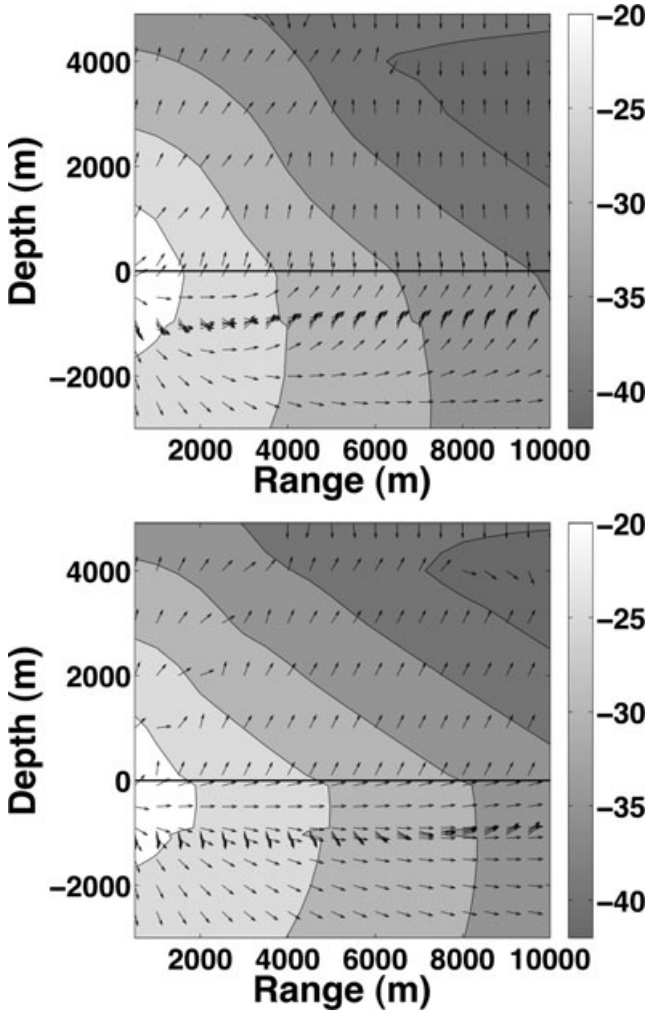

Figure 15. Contours of the logarithm of the magnitude of the real part of the complex Poynting vector (colours) and its local direction at the origin of each white arrow produced by a 1 Hz point HED source with a moment of 1 A-m located 50 m above the seafloor at a range of 0. The length of each arrow is identical, and the horizontal black line depicts the seafloor. The water depth H is 5000 m, and the subsurface electrical structure is the brine model of Fig. 1. The top panel shows the Poynting vector at an azimuth of 90°, whereas the lower panel shows it at an azimuth of 0°. In both instances, the horizontal component is in the radial direction.

shown. This is reflected in Fig. 15 (top), which closely resembles Fig. 9 (top) close to the source but is different from both that plot and Fig. 6 (top) beyond that point, where the flux from below the conductive layer to within the ocean layer is increasingly vertical as depth decreases. Further, comparison of the top and bottom panels of Fig. 15 shows that the in-line energy flux is larger than the parallel energy flux throughout the structure.

Fig. 16 shows the Poynting vector for a 1 Hz HED source and the weak hydrocarbon reservoir model in the in-line (bottom) and parallel (top) orientations. As for the brine reservoir, the in-line cross-section closely resembles that for the VED in Fig. 6 (bottom) and Fig. 7 (top), except that guided diffusion in the resistive layer is established very close to the source for the HED. In the parallel direction, the seafloor PM mode is larger than the TM mode at ranges under 12 000 m, although the difference is quite small beyond 6000 m. Fig. 16 (top) bears some resemblance to Fig. 9 (top) out to 6000 m range, and thereafter the Poynting vector is increasingly vertical with distance above the resistive layer. A decrease in the Poynting vector magnitude across the reservoir layer that grows with range is also evident. As for the brine model, the parallel direction Poynting vector is much weaker than the in-line one for a given range.

Fig. 17 shows the Poynting vector for a 1 Hz HED source and the strong hydrocarbon reservoir model. The in-line cross-section resembles that for the VED in Fig. 6 (bottom) and Fig. 7 (top) and the weak reservoir model in Fig. 16 (bottom), except that enhancement of the Poynting vector magnitude both within the reservoir layer and substrate at a given range is stronger. In the parallel direction, the seafloor PM mode is larger than the TM mode only at ranges below about 3000 m, and the TM mode becomes increasingly dominant with range beyond that point. Fig. 17 (top) resembles Fig. 16 (top) close to the source, but changes form around 3000 m range and then evolves into nearly vertical flow out of the reservoir layer both above and below it. Concomitantly, the Poynting vector magnitude displays a sharp minimum within the reservoir layer that grows with increasing range, energy flux in the ocean becomes nearly vertical, and the magnitude at a given range becomes

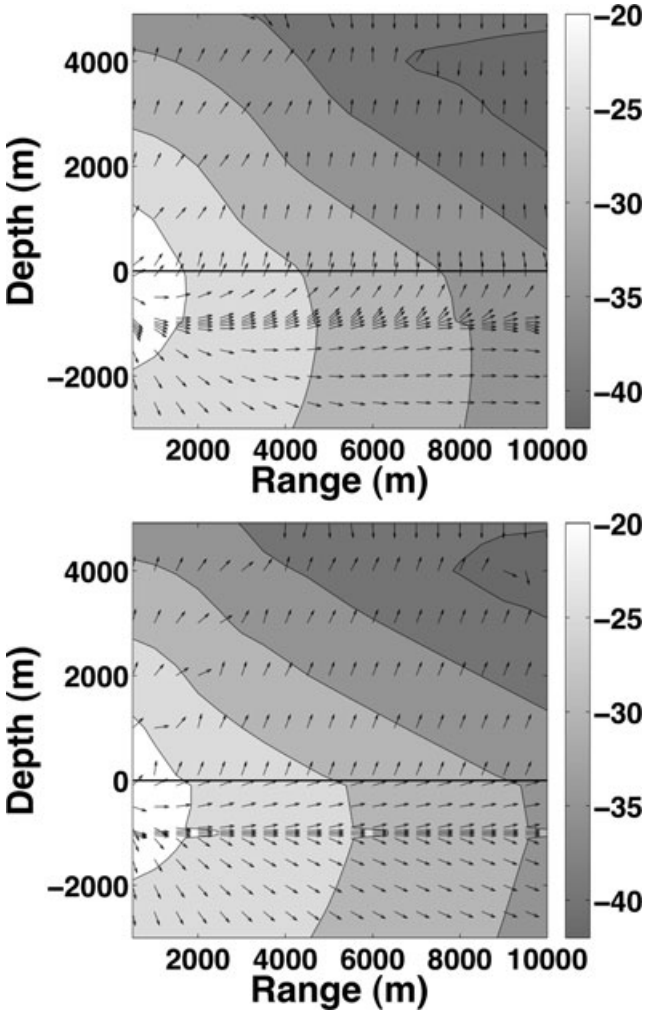

Figure 16. Contours of the logarithm of the magnitude of the real part of the complex Poynting vector (greyscale) and its local direction at the origin of each black arrow produced by a 1 Hz point HED source with a moment of 1 A-m located 50 m above the seafloor at a range of 0. The length of each arrow is identical, and the horizontal black line depicts the seafloor. The water depth H is 5000 m, and the subsurface electrical structure is the weak hydrocarbon reservoir model of Fig. 1. The top panel shows the Poynting vector at an azimuth of 90°, whereas the lower panel shows it at an azimuth of 0°. In both instances, the horizontal component is in the radial direction.

dramatically smaller than for the in-line orientation. The physical picture that emerges for the region where the TM mode is dominant is one of enhanced dissipation from the reservoir layer with no evidence for guided diffusion as in the in-line direction.

The observations about Figs 15–17 are consistent with the behaviour of the EM fields, and can be understood in terms of their changes across the subsurface structure. For the in-line direction, the Poynting vector is $(S_\rho, S_z) = (-E_z B_\phi^*, E_\rho B_\phi^*)/2\mu$. Fig. 18 shows profiles of the magnitude and phase of E_ρ, E_z and B_ϕ from the seafloor to the bottom of the model at ranges of 2000 and 8000 m, respectively. At both of these ranges, the TM mode is weakly (a factor of 2–5) larger than the PM mode for the horizontal field components except around 500 m depth for the brine and weak hydrocarbon models, whereas the TM mode is dominant everywhere for the strong hydrocarbon model. For the hydrocarbon reservoir structures, E_z is discontinuous at the reservoir boundary and increases within it because the vertical electric current density is continuous, whereas E_ρ is continuous at the reservoir boundary, decreases within it and undergoes a nearly 180° phase change across the layer. B_ϕ is continuous and less dependent on the conductivity jump. Because E_z is substantially larger than E_ρ, the in-line Poynting vector is nearly horizontal within the reservoir and its vertical component changes sign across it, consistent with Figs 16 and 17 (bottom). E_ρ and B_ϕ for the brine model are similar to those for a half-space, whereas E_z displays a minimum at the layer due to continuity of vertical electric current density. Consequently, S_ρ is at a minimum in the brine layer, and there is no guided diffusion.

For the parallel direction, the Poynting vector is $(S_\rho, S_z) = (E_\phi B_z^*, -E_\phi B_\rho^*) / 2\mu$. At 2000 m range (Fig. 19, top panels), the horizontal fields are the result of a complex interplay between the TM and PM modes. At 8000 m range (Fig. 19, bottom panels), the E_ϕ TM mode is much larger than the PM mode for all models, whereas B_ρ is the result of depth-varying interplay between the modes except for the strong hydrocarbon model, where the TM mode is dominant. E_ϕ displays a change of sign across both hydrocarbon reservoirs, resulting in a sharp minimum in the Poynting vector that is especially apparent for the strong hydrocarbon model. At 2000 m range, B_ρ is comparable to B_z near

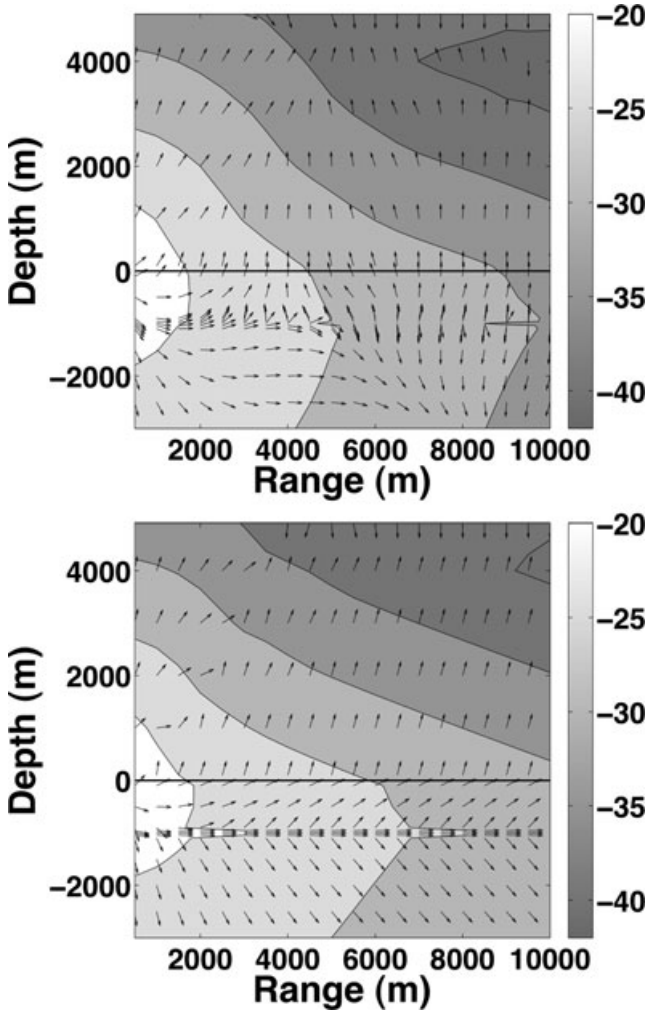

Figure 17. Contours of the logarithm of the magnitude of the real part of the complex Poynting vector (greyscale) and its local direction at the origin of each black arrow produced by a 1 Hz point HED source with a moment of 1 A-m located 50 m above the seafloor at a range of 0. The length of each arrow is identical, and the horizontal black line depicts the seafloor. The water depth H is 5000 m, and the subsurface electrical structure is the strong hydrocarbon reservoir model of Fig. 1. The top panel shows the Poynting vector at an azimuth of 90°, whereas the lower panel shows it at an azimuth of 0°. In both instances, the horizontal component is in the radial direction.

the reservoir, whereas B_ρ is substantially larger than B_z at 8000 m. As a result, the parallel direction Poynting vector is nearly vertical and changes sign across the layer, consistent with Figs 16 and 17 (top).

Finally, the Poynting vector and seafloor field behaviour from an HMD source is very similar to that for an HED source. This ought not to be a surprise given that an HED of a given length is an approximation to an HMD with the same diameter, as most of the return current from the bared ends of the HED flows in the water. This does raise the issue of whether an HMD might offer practical advantages over an HED in terms of deployment ease, source moment, ability to maintain azimuth and accuracy of the point source approximation that require further investigation.

11 CONCLUSIONS

This paper presents a comprehensive framework for the solution of 1-D EM induction problems in terms of independent modes that separate the salient physics into two distinct types. It also provides solutions for finite versions of the four fundamental sources along with their point limits. It is hoped that collecting this information in a single place will serve both pedagogic and practical purposes.

Throughout the paper, emphasis has been placed on the diffusional nature of the EM field in marine CSEM. This is more than a pedantic point, as the use of wave propagation analogies for diffusion can lead to incorrect physical insight. Further, basing the theory on the governing diffusion physics rather than the full Maxwell equations results in considerable conceptual and mathematical simplification, as may be seen through comparison to Løseth *et al.* (2006) and Amundsen *et al.* (2006). This reflects the fact that inclusion of displacement current in the governing equations, and the mathematical complexity that ensues, does not imply that wave propagation phenomena are present in the physics.

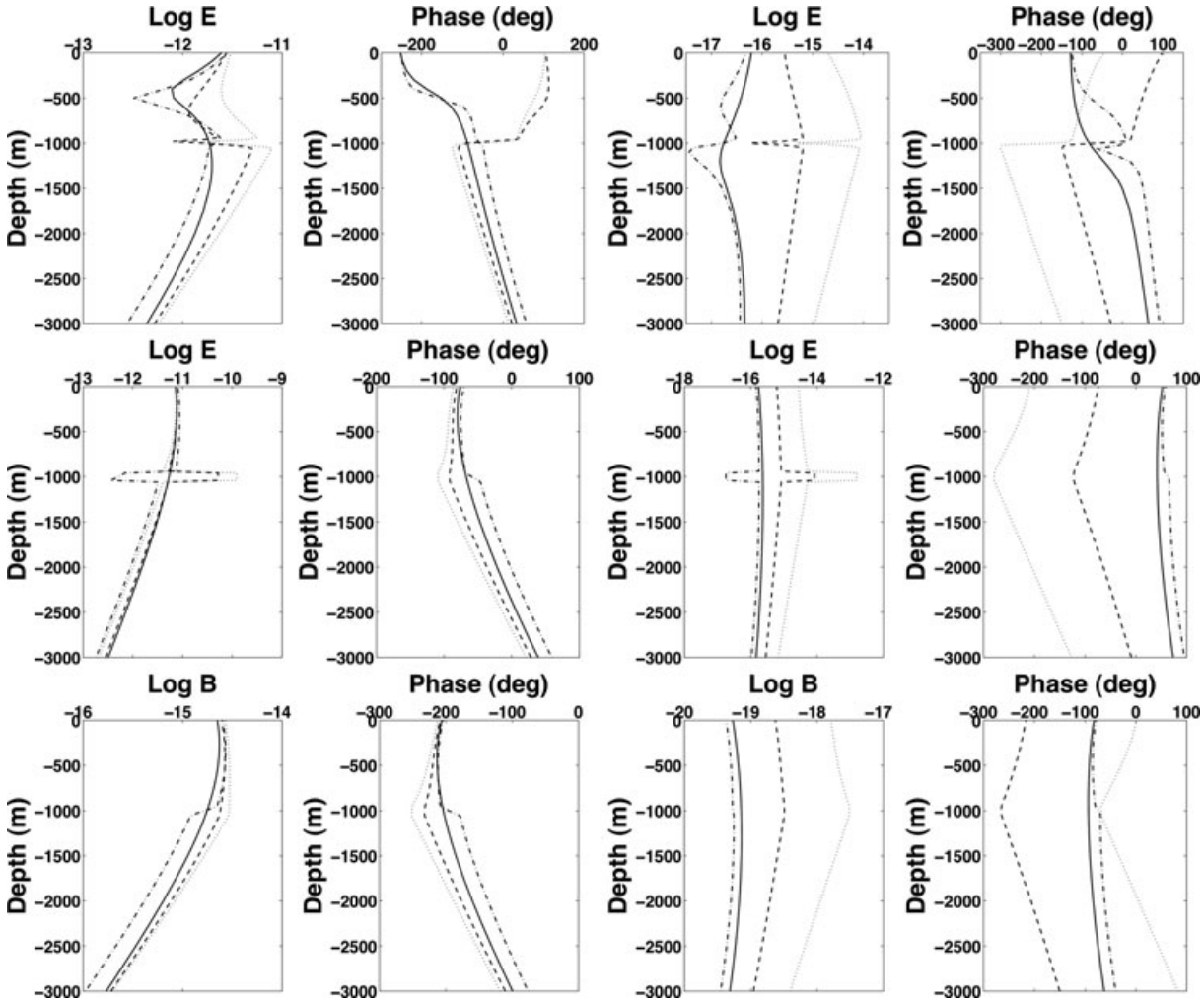

Figure 18. From top to bottom, the logarithm of the amplitude and the phase of the radial and vertical electric, and azimuthal magnetic fields from the seafloor to the base of the model structure at 2000 m range (first six panels) and 8000 m range (last six panels), as produced by a unit HED source at 50 m height above the seafloor at the origin and at an azimuth of 0°. The four models shown are a uniform half-space (solid line), the brine model (dash-dot line), the weak hydrocarbon model (dashed line) and the strong hydrocarbon model (dotted line).

In Section 8 and Figs 12–14, evidence has been presented that a single component view of marine CSEM fields is insufficient, and that in fact the three Cartesian components are interdependent in a complicated manner. Even when the elliptical polarization of the EM field is taken into account, it is difficult to obtain much insight into marine CSEM from field behaviour only at the seafloor. Nevertheless, it is clear that there is information in triaxial as opposed to only horizontal measurements of the EM field. It has also been shown that, leaving aside possible signal-to-noise considerations, there is limited gain from augmenting either electric or magnetic field data with the conjugate quantity for a given source–receiver offset. However, because the electric and magnetic fields respond differently for a given source–receiver orientation, there may be value in measuring both quantities in practical surveys where a wide range of source–receiver geometries occur.

A core theme of this paper is that understanding the physics of marine CSEM requires insight into the flow of energy in the subsurface structure through visualization of the Poynting vector. Section 9 and Figs 6–10 present that quantity for unimodal VED and VMD sources, showing graphically that, for the TM mode, a thin resistive layer serves as the locus for horizontal energy channeling with concomitant leakage into more conductive regions, leading to enhancement of the seafloor EM field compared to models without resistive zones. In contrast, a conductive zone results only in field attenuation through increased Joule heating. The PM mode is quite insensitive to a thin resistive layer, and is attenuated by dissipation in a conductive zone. It is also strongly influenced by the so-called air wave diffusing along the sea surface, whereas the TM mode is unaffected. None of these results are new, but their presentation in the form of the Poynting vector provides a basic grounding for marine CSEM physics that has heretofore been obscure.

For the bimodal HED and HMD sources, the Poynting vector does not separate into TM and PM mode components, and hence insight from the unimodal sources is needed to understand the energy flow. Additional complexity ensues from the azimuthal dependence of the EM field that is reflected in the Poynting vector. However, it is only necessary to consider it in the in-line and parallel configurations to understand energy flow for any source–receiver orientation, and those results have been analyzed in Section 10.

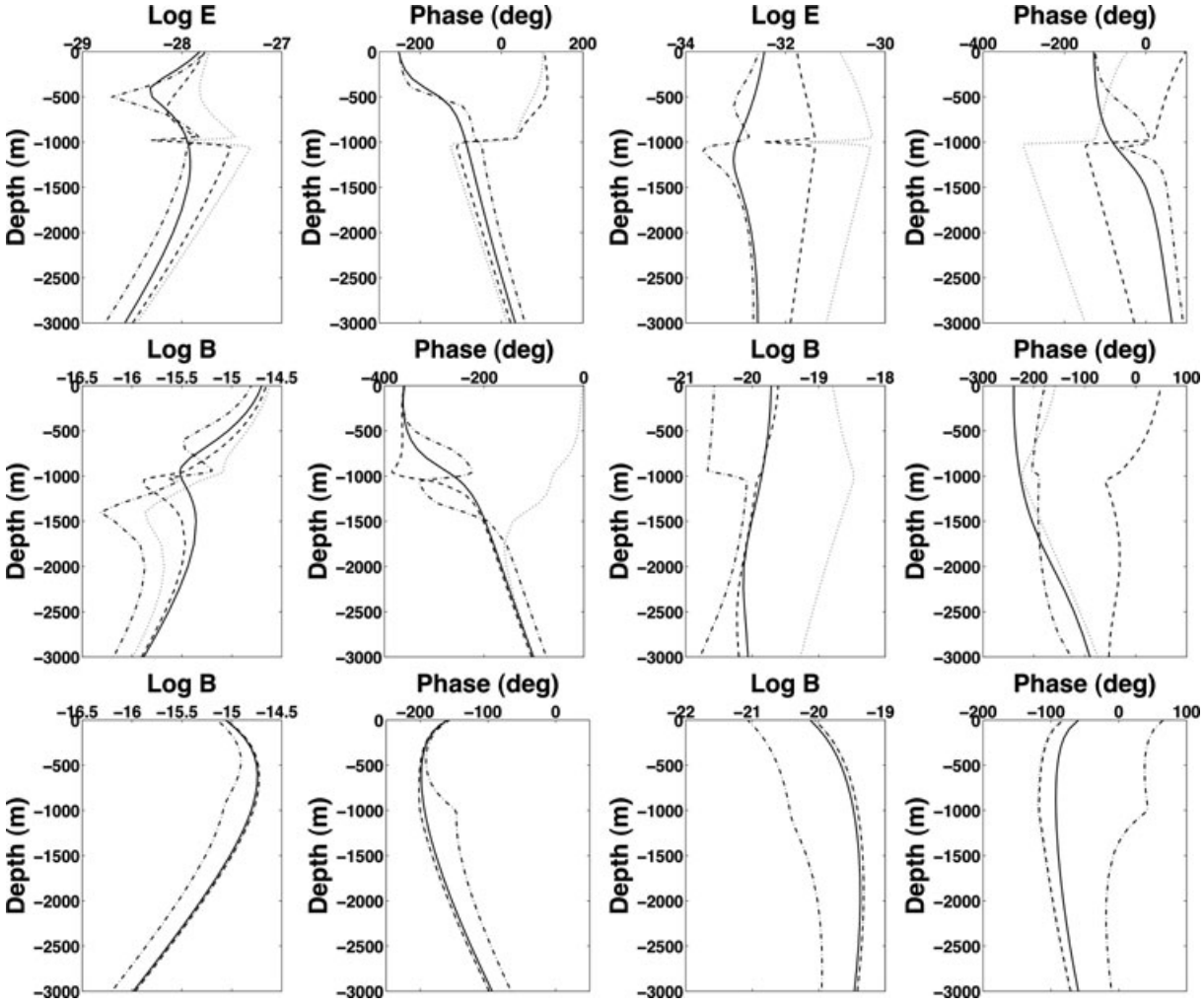

Figure 19. From top to bottom, the logarithm of the amplitude and the phase of the azimuthal electric, and radial and vertical magnetic fields from the seafloor to the base of the model structure at 2000 m range (first six panels) and 8000 m range (last six panels), as produced by a unit HED source at 50 m height above the seafloor at the origin and at an azimuth of 90°. The four models shown are a uniform half-space (solid line), the brine model (dash-dot line), the weak hydrocarbon model (dashed line) and the strong hydrocarbon model (dotted line).

Finally, extension of the Poynting vector analysis to 2-D and 3-D structures would be of considerable benefit to both students and petroleum industry practitioners. Such calculations could be obtained fairly easily from existing numerical simulation codes.

ACKNOWLEDGMENTS

This paper is the direct result of the author's service as an expert witness in a patent dispute in the High Court of Justice, London, during which it became clear that misconceptions about the physics of marine CSEM were pervasive, especially in patents. The author wishes to acknowledge many valuable discussions with Justin Watts and Paul Joseph, solicitors with Freshfields Druckhaus Derringer, and Michael Silverleaf, QC, and Hugo Cuddigan, barristers, that contributed to the content. He also wishes to acknowledge the efforts of two anonymous reviewers and Peter Weidelt, whose comments contributed substantially to the presentation. Completion was supported by NSF grant OCE-0221832. This paper is dedicated with respect to the memory of Peter Weidelt, colleague and friend, whose intellect and humanity will surely be missed.

REFERENCES

Amundsen, H.E.F., Løseth, L., Mittet, R., Ellingsrud, S. & Ursin, B., 2006. Decomposition of electromagnetic fields into upgoing and downgoing components, *Geophysics,* **71,** G211–G223.

Backus, G.E., 1986. Poloidal and toroidal fields in geomagnetic modeling, *Rev. Geophys.,* **24,** 75–109.

Bannister, P.R., 1968. Determination of the electrical conductivity of the seabed in shallow water, *Geophysics,* **33,** 995–1003.

Berdichevsky, M., 1994. Role of geoelectrical methods in hydrocarbon and deep structural investigations in Russia, *Geophys. Trans.,* **39,** 3–33.

Born, M. & Wolf, E., 2002. *Principles of Optics*, Cambridge University Press, Cambridge, 952 pp.

Chave, A.D., 1983. Numerical integration of related Hankel transforms by quadrature and continued fraction expansion, *Geophysics,* **48,** 1671–1686.

Chave, A.D. & Cox, C.S., 1982. Controlled electromagnetic sources for measuring electrical conductivity beneath the oceans, 1, forward problem and model study, *J. geophys. Res.,* **87,** 5327–5338.

Chave, A.D. & Luther, D.S., 1990. Low frequency, motionally induced electromagnetic fields in the ocean, 1, Theory, *J. geophys. Res.,* **95,** 7185–7200.

Chave, A.D., Flosadottir, A. & Cox, C.S., 1990. Some comments on seabed propagation of ULF/ ELF electromagnetic fields, *Radio Sci.,* **25,** 825–836.

Chave, A.D., Constable, S.C. & Edwards, R.N., 1991. Electrical exploration methods for the seafloor, in *Electromagnetic Methods in Applied Geophysics*, Vol. 2, pp. 931–966, ed. Nabighian, M.N., Society of Exploration Geophysicists, Tulsa.

Cheesman, S.J., Edwards, R.N. & Chave, A.D., 1987. On the theory of seafloor conductivity mapping using transient electromagnetic systems, *Geophysics,* **52,** 204–217.

Coggon, J.H. & Morrison, H.F., 1970. Electromagnetic investigation of the seafloor, *Geophysics,* **35,** 476–489.

Constable, S.C. & Cox, C.S., 1996. Marine controlled-source electromagnetic sounding 2. The PEGASUS experiment, *J. geophys. Res.,* **101,** 5519–5530.

Constable, S.C. & Weiss, C.J., 2006. Mapping thin resistors and hydrocarbons with marine EM methods: insights from 1D modeling, *Geophysics,* **71,** G43–G51.

Constable, S.C. & Srnka, L.J., 2007. An introduction to marine controlled-source electromagnetic methods for hydrocarbon exploration, *Geophysics,* **72,** WA3–WA12.

Cox, C.S. & Chave, A.D., 1983. Controlled source electromagnetic exploration of the continental shelves and oceanic lithosphere, *Proc. 1983 Int. Symp. Ant. Prop.,* **21,** 475–477.

Cox, C.S., Kroll, N., Pistek, P. & Watson, K., 1978. Electromagnetic fluctuations induced by wind waves on the deep-sea floor, *J. geophys. Res.,* **83,** 431–442.

Cox, C.S., Constable, S.C., Chave, A.D. & Webb, S.C., 1986. Controlled-source electromagnetic sounding of the oceanic lithosphere, *Nature,* **320,** 52–54.

Dey, A. & Ward, S.H., 1970. Inductive sounding of a layered Earth with a horizontal magnetic dipole, *Geophysics,* **35,** 660–703.

Edwards, R.N., 2005. Marine controlled source electromagnetics: principles, methodologies, future commercial applications, *Surv. Geophys.,* **26,** 675–700.

Edwards, R.N., Law, L.K. & DeLaurier, J.M., 1981. On measuring the electrical conductivity of the oceanic crust by a modified magnetometric resistivity method, *J. geophys. Res.,* **86,** 11 609–11 615.

Edwards, R.N., Law, L.K., Wolfgram, P.A., Nobes, D.C., Bone, M.N., Trigg, D.F. & DeLaurier, J.M., 1985. First results of the MOSES experiment: sea sediment conductivity and thickness determination, Bute Inlet, British Columbia, by magnetometric offshore electrical sounding, *Geophysics,* **50,** 153–161.

Edwards, R.N., Wolfgram, P.A. & Judge, A.S., 1988. The ICE-MOSES experiment: mapping permafrost zones electrically beneath the Beaufort Sea, *Mar. Geophys. Res.,* **9,** 265–290.

Ellingsrud, S., Eidesmo, T., Johansen, S., Sinha, M.C. MacGregor, L.M. & Constable, S., 2002. Remote sensing of hydrocarbon layers by seabed logging (SBL): results from a cruise offshore Angola, *Leading Edge,* **21,** 972–982.

Evans, R.L., 2007. Using CSEM techniques to map the shallow section of the seafloor: from the coastline to the edges of the continental shelf, *Geophysics,* **72,** WA105–WA116.

Evans, R.L., Webb, S.C., Jegen, M. & Sananikone, K., 1998. Hydrothermal circulation at the Cleft-Vance overlapping spreading center: results of a magnetometric resistivity survey, *J. geophys. Res.,* **103,** 12 321—12 338.

Garg, N.R. & Keller, G.V., 1984. Synthetic electric sounding surveys over known oil fields, *Geophysics,* **49,** 1959–1967.

Horton, C.W., 1946. On the use of electromagnetic waves in geophysical prospecting, *Geophysics,* **9,** 505–518.

Johansen, S.E., Amundsen, H.E.F., Røsten, T., Ellingsrud, S., Eidesmo, T. & Bhuyian, A.H., 2005. Subsurface hydrocarbons detected by electromagnetic sounding, *First Break,* **23,** 31–36.

Keller, G.V., Jordan, J.M. & Tasci, M.T., 1995. Case histories using time domain electromagnetics in oil and gas exploration: from inversion to imaging, *SEG Ext. Abstr.,* **14,** 222–225.

Løseth, L.O., Pedersen, H.M., Ursin, B., Amundsen, L. & Ellingsrud, S., 2006. Low frequency electromagnetic fields in applied geophysics: waves or diffusion?, *Geophysics,* **71,** W29–W40.

MacGregor, L.M., Constable, S. & Sinha, M.C., 1998. The RAMESSES experiment III. Controlled-source electromagnetic sounding of the Reykjanes Ridge at 57°45′N, *Geophys. J. Int.,* **135,** 773–789.

MacGregor, L.M., Sinha, M.C. & Constable, S., 2001. Electrical resistivity structure of the Valu Fa Ridge, Lau Basin, from marine controlled-source electromagnetic sounding, *Geophys. J. Int.,* **146,** 217–236.

Mandelis, A., 2006. *Diffusion Wave Fields: Green Functions and Mathematical Methods*, Springer-Verlag, Berlin, 741 pp.

Mandelis, A., Nicolaides, L. & Chen, Y., 2001. Structure and the reflectionless/refractionless nature of parabolic diffusion-wave fields, *Phys. Rev. Lett.,* **87,** 020801.

Martin, M., Murray, G.H. & Gillingham, W.J., 1938. Determination of the potential productivity of oil-bearing formations by resistivity measurements, *Geophysics,* **3,** 258–272.

Meju, M., 2002. Geoelectromagnetic exploration for natural resources: models, case studies and challenges, *Surv. Geophys.,* **23,** 133–205.

Mott, H. & Biggs, A.W., 1963. Very low frequency propagation below the bottom of the sea, *IEEE Trans. Antennas Propag.,* **AP-11,** 323–329.

Nekut, A.G. & Spies, B.R., 1989. Petroleum exploration using controlled-source electromagnetic methods, *Proc. IEEE,* **77,** 338–362.

Oehler, D.Z. & Sternberg, B.K., 1984. Seepage-induced anomalies, "false" anomalies, and implications for electrical prospecting, *Am. Assoc. Petrol. Geol. Bull.,* **68,** 1121–1145.

Passalaqua, H., 1983. Electromagnetic fields due to a thin resistive layer, *Geophys. Prospect.,* **31,** 945–976.

Srnka, L., 1986. Method and apparatus for offshore electromagnetic sounding utilizing wavelength effects to determine optimum source and detector positions, *U.S. Patent*, *4,617,518*.

Spies, B., 1983. Recent developments in the use of surface electrical methods for oil and gas exploration in the Soviet Union, *Geophysics,* **48,** 1102–1112.

Strack, K.-M. & Vozoff, K., 1996. Integrating long-offset transient electromagnetics (LOTEM) wth seismics in an exploration environment, *Geophys. Prospect.,* **44,** 997–1017.

Um, E.S. & Alumbaugh, D.L., 2007. On the physics of the marine controlled-source electromagnetic method, *Geophysics,* **72,** WA13–WA26.

Weidelt, P., 2007. Guided waves in marine CSEM, *Geophys J. Int.,* **171,** 153–176.

Weiss, C.J., 2007. The fallacy of the "shallow-water problem" in marine CSEM exploration, *Geophysics,* **72,** A93–A97.

Yost, W.J., 1952. The interpretation of electromagnetic reflection data in geophysical exploration—Part 1, general theory, *Geophysics,* **17,** 89–106.

Young, P.D. & Cox, C.S., 1981. Electromagnetic active source sounding near the East Pacific Rise, *Geophys. Res. Lett.,* **8,** 1043–1046.

Yuan, J. & Edwards, R.N., 2000. The assessment of marine gas hydrates through electrical remote sounding: hydrate without a BSR?, *Geophys. Res. Lett.,* **27,** 2397–2400.

APPENDIX: DERIVATION OF THE MODAL EQUATIONS

Using the Helmholtz representation theorem, any vector field may be written in terms of its toroidal, consoidal and vertical parts

$$\mathbf{T} = \hat{z} \times \nabla_h r + \nabla_h s + t\hat{z}, \tag{A1}$$

where r, s and t are scalar functions and $\langle r\rangle = \langle s\rangle = 0$ using (9). By virtue of (3), a condition on the Helmholtz representation of the magnetic induction is $\nabla_h^2 s + \partial_z t = 0$. This condition may be satisfied by choosing $r = \Pi$, $s = \partial_z \Psi$ and $t = -\nabla_h^2 \Psi$, yielding (10). This is equivalent to the familiar vector potential with $\mathbf{A} = (\partial_y \Psi, -\partial_x \Psi, -\Pi)$ and $\mathbf{B} = \nabla \times \mathbf{A}$. The scalar functions Ψ and Π represent poloidal and toroidal magnetic modes for which governing differential equations will be derived using (4) and (5) combined with a Helmholtz representation of the electric field

$$\mathbf{E} = \hat{z} \times \nabla_h \alpha + \nabla_h \beta + \gamma \hat{z}, \tag{A2}$$

and the source current density (6).

Substituting (10) and (A2) into Faraday's Law (4), assuming $e^{-i\omega t}$ time dependence and writing out the three components yields

$$\begin{aligned}
&\partial_x (-\partial_z \alpha - i\omega \partial_z \Psi) - \partial_y (-\gamma + \partial_z \beta - i\omega \Pi) = 0 \\
&\partial_y (-\partial_z \alpha - i\omega \partial_z \Psi) + \partial_x (-\gamma + \partial_z \beta - i\omega \Pi) = 0 \\
&\nabla_h^2 (i\omega \Psi + \alpha) = 0.
\end{aligned} \tag{A3}$$

The first two equations are the Cauchy–Riemann conditions. Taking

$$\begin{aligned}
u_1 &= -\partial_z \alpha - i\omega \partial_z \Psi \\
v_1 &= -\gamma + \partial_z \beta - i\omega \Pi,
\end{aligned} \tag{A4}$$

these require

$$u_1 + i v_1 = f_1 (x + iy) \tag{A5}$$

where f_1 is an analytic function of a complex variable, and u_1 and v_1 are harmonic.

Any transformation may be made to the modal scalar functions provided that the pre-Maxwell equations are not violated and the fields are unchanged. Let $\Psi = \Psi' - \upsilon$, where $\upsilon = \Psi + \alpha/i\omega$. Substituting into (10) yields

$$\mathbf{B} = \hat{z} \times \nabla_h \Pi + \nabla_h \partial_z \Psi' - \nabla_h \partial_z \upsilon - \nabla_h^2 \Psi' \hat{z} + \nabla_h^2 \upsilon \hat{z}, \tag{A6}$$

where the final term vanishes because of the last equation in (A3). Consequently, writing $\Pi = \Pi' + \varsigma$ and choosing ς such that $\hat{z} \times \nabla_h \varsigma = \nabla_h \partial_z \upsilon$ yields (10), and hence υ may have been taken as zero from the outset. Because $u_1 = \partial_z \upsilon$, that quantity is also zero, and hence v_1 is a constant (i.e. independent of x and y). However, a constant may be added to Π in the second term of (A4) without changing (10), and hence v_1 may also be taken as zero. This establishes two conditions on α, β and γ.

Repeating the same procedure using Ampere's Law (5) yields

$$\begin{aligned}
&\partial_x(\nabla^2 \Psi - \mu\sigma\alpha - \mu\Upsilon) - \partial_y(\partial_z \Pi + \mu\sigma\beta + \mu T) = 0 \\
&\partial_y(\nabla^2 \Psi - \mu\sigma\alpha - \mu\Upsilon) + \partial_x(\partial_z \Pi + \mu\sigma\beta + \mu T) = 0 \\
&\nabla_h^2 \Pi - \mu\sigma\gamma - \mu\Xi = 0.
\end{aligned} \tag{A7}$$

The first two equations are again the Cauchy–Riemann conditions. Defining

$$\begin{aligned}
u_2 &= \nabla^2 \Psi - \mu\sigma\alpha - \mu\Upsilon \\
v_2 &= \partial_z \Pi + \mu\sigma\beta + \mu T,
\end{aligned} \tag{A8}$$

these require

$$u_2 + i v_2 = f_2 (x + iy), \tag{A9}$$

where f_2 is an analytic function. Because (10) is independent of $\partial_z \Pi$, that quantity may be chosen arbitrarily (note that this is functionally equivalent to the choice of gauge through specifying $\nabla \cdot \mathbf{A}$ for the ordinary vector potential), and hence v_2 may be taken as zero. This means that u_2 is independent of x and y, but a constant may be added to Υ in (6) without changing the source current density, and hence u_2 is also zero. Combining the terms yields the electric field (11) and the frequency domain version of the modal differential eqs (12) and (13).